

Article

Oxygen Deficiency and Migration-Mediated Electric Polarization in Magnetic Fe,Co-Substituted $\text{SrTiO}_{3-\delta}$

Emilio A. Cortés Estay ¹, Shyue P. Ong ², Caroline A. Ross ³ and Juan M. Florez ^{1,3,*}

¹ Grupo de Simulaciones, Departamento de Física, Universidad Técnica Federico Santa María, Casilla 110-V, Valparaíso 2390123, Chile

² Department of NanoEngineering, University of California, San Diego, 9500 Gilman Drive, La Jolla, CA 92093, USA

³ Department of Materials Science and Engineering, Massachusetts Institute of Technology, 77 Massachusetts Avenue, Cambridge, MA 02139, USA

* Correspondence: juanmanuel.florez@usm.cl or jmflorez@mit.edu

Abstract: We use density functional theory (DFT) calculations to show that oxygen vacancies (v_{O}) and mobility induce noncentrosymmetric polar structures in $\text{SrTi}_{1-x-y}\text{Fe}_x\text{Co}_y\text{O}_{3-\delta}$ (STFC, $x = y = 0.125$) with $\delta = \{0.125, 0.25\}$, enhance the saturation magnetization, and give rise to large changes in the electric polarization $|\Delta P|$. We present an intuitive set of rules to describe the properties of STFC, which are based on the interplay between (Co/Fe)- v_{O} defects, magnetic cation coordination, and topological vacancy disorder. STFC structures consist of layered crystals with sheets of linearly organized $\text{O}_{4,5,6}$ -coordinated Fe–Co pairs, sandwiched with layers of O_5 -coordinated Ti. (Co/Fe)- v_{O} defects are the source of crystal distortions, cation off-centering and bending of the oxygen octahedra which, considering the charge redistribution mediated by v_{O} and the cations' electronegativity and valence states, triggers an effective electric polarization. Oxygen migration for $\delta = 0.125$ leads to $|\Delta P| > \sim 10 \mu\text{C}/\text{cm}^2$ due to quantum-of-polarization differences between $\delta = 0.125$ structures. Increasing the oxygen deficiency to $\delta = 0.25$ yields $|\Delta P|$, the O migration of which resolved polarization for $\delta = 0.25$ is $> \sim 3 \mu\text{C}/\text{cm}^2$. Magnetism is dominated by the Fe,Co spin states for $\delta = 0.125$, and there is a contribution from Ti magnetic moments ($\sim 1 \mu_B$) for $\delta = 0.25$. Magnetic and electric order parameters change for variations of δ or oxygen migration for a given oxygen deficiency. Our results capture characteristics observed in the end members of the series $\text{SrTi}(\text{Co,Fe})\text{O}_3$, and suggest the existence of a broader set of rules for oxygen-deficient multiferroic oxides.

Keywords: multiferroic materials; magnetic perovskites; oxygen vacancy; density functional theory



Citation: Cortés Estay, E.A.; Ong, S.P.; Ross, C.A.; Florez, J.M. Oxygen Deficiency and Migration-Mediated Electric Polarization in Magnetic Fe,Co-Substituted $\text{SrTiO}_{3-\delta}$. *Magnetochemistry* **2022**, *8*, 144. <https://doi.org/10.3390/magnetochemistry8110144>

Academic Editor: Roberto Zivieri

Received: 7 September 2022

Accepted: 24 October 2022

Published: 1 November 2022

Publisher's Note: MDPI stays neutral with regard to jurisdictional claims in published maps and institutional affiliations.



Copyright: © 2022 by the authors. Licensee MDPI, Basel, Switzerland. This article is an open access article distributed under the terms and conditions of the Creative Commons Attribution (CC BY) license (<https://creativecommons.org/licenses/by/4.0/>).

1. Introduction

Materials that simultaneously possess at least two ferroic orders (ferroelectricity, ferroelasticity, and/or ferro/ferri/antiferromagnetism) are described as multiferroic [1]. The search for such materials has expanded to several classes of systems, of which the magnetic perovskites provide outstanding examples with a wide range of cation compositions and oxygen stoichiometries [1–3]. Among transition metal (TM) perovskites, $\text{SrTi}_{1-x}\text{Fe}_x\text{O}_{3-\delta}$ (STF) and $\text{SrTi}_{1-x}\text{Co}_x\text{O}_{3-\delta}$ (STC) both display magnetization that depends on their oxygen content, with typically higher magnetization at higher levels of oxygen deficiency (δ) [4–6]. On the other hand, at room temperature, stoichiometric SrTiO_3 (STO) is a nonmagnetic paraelectric. At low temperatures, it presents an antiferrodistortive structural change that suppresses the ferroelectric (FE) ordering, as well as quantum fluctuations that forbid the FE phase transition [7–9]. Several mechanisms promote a FE phase in STO [10,11]. For example, the application of electric fields, A-site cation substitution, strain in thin films [12,13] and nonstoichiometric solid solutions have all been proposed to lead to a ferroelectric response [14,15]. Defects such as coupled Sr (v_{Sr}) and O (v_{O}) vacancies, v_{Sr} with interstitial I_{Ti} , anti-site Ti_{Sr} and Sr_{Ti} and their coupling with v_{O} [16–18] have been suggested

to promote ferroelectricity in STO with Sr/Ti atomic ratio close to 1 [19]. A-site defects such as v_{Sr} can also mediate polar effects in (111)-oriented and (001)-bulk-terminated perovskites based on SrTiO_3 [20,21].

Oxygen deficiency has been used to enhance multiferroicity in PbTiO_3 [22] and ferroelectric switching in Si-doped HfO_2 [23]. Ferroic parameters in YMnO_3 [24] and strained SrMnO_3 [25] could be manipulated by using δ as well as the ferroelectric response in perovskite-structured relaxors [26]. Multiferroism in oxygen-deficient SrFeO_3 nanoparticles was also studied [27], and the magnetic ordering followed the tendencies of the v_{O} -modulated magnetism in STF [4], whereas the FE parameter was not clearly associated with the v_{O} . STF also displays ferroelectricity in nanocrystalline thin-film form with a polarization up to $6 \mu\text{C}/\text{cm}^2$ depending on the Fe concentration [28]. In addition, a comparable field-driven polarization of up to $\sim 1 \mu\text{C}/\text{cm}^2$ was realized in Fe-doped, Ti-rich STO multiferroics at room temperature [29]. In the case of STC, although its FE properties have not been reported, preliminary work [30] suggests that STC could share some FE characteristics with O-deficient STO. STC presents a relatively large band gap and room temperature magnetization [31,32] as well as off-centering features induced by the incorporation of Co [33] or through the Co- v_{O} -Ti distortions [34], which are ingredients of the STO-like ferroicity discussed in this work.

The use of oxygen deficiency as a tool with which to tailor ferroic order parameters requires a profound knowledge of the roles of the defect density and vacancy distributions, ABO_3 cation symmetry and ratio, as well as of the TM electronic features such as valence states, radii, electronegativity, stabilizing hybridizations, and occupancies [4,5,34]. Although physical/chemical synthesis is able to control several of these factors [4,34], obtaining specific polarization/magnetization values requires theoretical and simulation insights that can help both to narrow the large parameter space of stoichiometries and compositions to achieve useful properties and to understand the microscopic mechanisms that underlie the origin of such ferroic orders in oxygen-deficient perovskites. In this work, we theoretically explore the perovskite $\text{SrTi}_{1-x-y}\text{Fe}_x\text{Co}_y\text{O}_{3-\delta}$ (STFC) [34] from three perspectives: the effect of different δ values with several v_{O} distributions for each δ ; substituting B cations with Fe and Co in distinct configurations, and modulating the TM spin states among the possible valence states and spin polarizations. STFC-based systems have been experimentally studied in the context of oxygen transport in membranes [35], electrical conductivity in energy applications and memristors [36], as well as oxygen electrodes for solid oxide cells [36,37]. The ferroelectric features of STFC have not been addressed, although there are indications of multiferroicity in this versatile material as we shall show here.

In Fe-substituted STO, the saturation magnetization can be modulated, and ferroelectric properties are induced for low x values ($\text{Fe}_x, y = 0$) [4,29]. STF tends toward stable antiferromagnetic solutions for low and high δ values, whereas Co-substituted STO is predominantly ferromagnetic for low O deficiencies without a Fe substitution ($\text{Co}_y, x = 0$) [4–6,38]. The STC band gap increases with δ , with presumably small but finite electric polarizations [5,30]; STFC presents an oxygen deficiency-modulated band gap that is maximum at intermediate δ along with the saturation magnetization [34]. On the other hand, $\text{SrFe}_{1-z}\text{Co}_z\text{O}_{3-\delta}$, without the nonmagnetic role of Ti, is able to display voltage-tuned magnetic response [39], which for low z values also displays multiferroicity [27]. All these factors suggest that Fe/Co-substituted STO could combine magnetic and ferroelectric order parameters within a realizable range of oxygen deficiency. Moreover, STFC could help to better understand the role of δ in the triggering of multiferroic behavior. That is, mechanisms known so far for proper or/and improper ferroelectricity [1–3] do not seem to completely account for several features of oxygen-deficient $\text{ABO}_{3-\delta}$. Therefore, computational engineering of oxygen-deficient compositions could show us one path toward designing room-temperature multiferroics. Furthermore, studies of order and coordination of TM cations have recently given new insights into multiferroic properties [4,5,34,39,40], voltage decay in Li-ion batteries [41,42], oxygen diffusion in strained oxides [43], and or-

dering in niobium–tungsten complex oxides [44], pointing to the importance of the local cation order in these materials.

In this work, we primarily focus on the ferroelectric and magnetic response of oxygen-deficient STFC. We demonstrate this by using density functional theory (DFT) calculations that oxygen vacancies (v_{O}) in $\text{SrTi}_{0.75}\text{Fe}_{0.125}\text{Co}_{0.125}\text{O}_{3-\delta}$ with $\delta = \{0.125, 0.25\}$ induce noncentrosymmetric polar structures, which support large electric polarization changes $|\Delta\mathbf{P}|$ through v_{O} migration and/or O-deficiency changes that are compatible with a robust magnetization. We explore a variety of v_{O} configurations and show how $|\Delta\mathbf{P}|$ varies within $\sim 23 \mu\text{C}/\text{cm}^2$ for the lowest-energy structures, with $\delta = 0.125$ systems displaying the highest resolved polarization differences. Our results capture key aspects of recent results on Fe–Co-substituted STO, and give a further insight into the electronic and structural mechanisms that would enable the realization of multiferroics by using specific defects and/or cation distributions in $\text{ABO}_{3-\delta}$.

2. DFT Modeling

Spin-polarized DFT calculations were performed by using the Vienna Ab-initio Simulation Package (VASP 5.4) [45] within the projector-augmented wave (PAW) method [46] and with an energy cutoff of 500 eV. k -point grids of $4 \times 4 \times 4$ for relaxation calculations as well as $6 \times 6 \times 6$ k -points for static calculations were used. The valence electrons included in the chosen pseudopotentials for Sr, Ti, Fe, Co, and O are $4s^2 4p^6 5s^2$, $3d^3 4s^1$, $3d^7 4s^1$, $3d^8 4s^1$, and $2s^2 2p^4$, respectively.

All ions and supercell parameters were relaxed until atomic forces were below 0.05 and 0.01 eV/Å, for large and intermediate δ values, respectively. Oxygen-migration barriers were computed by using the nudged elastic band (NEB) method [47], with forces converged below 100 meV/Å and energies below 10^{-5} eV. The generalized gradient approximation (GGA) within the Dudarev approach for the $+U$ -corrected Hubbard model (GGA+U) was used for the d electrons of the TM [48].

The U values used here for Fe, Co, and Ti are 3, 9, and 8 eV, respectively, and were chosen based on an extensive search for lattice parameters, local magnetic moments, and band-gap behaviors that would best represent end members SrTiO_3 , SrFeO_3 and SrCoO_3 , as well as the intermediate solutions $\text{SrTi}_{1-x}\text{Fe}_x\text{O}_3$ and $\text{SrTi}_{1-x}\text{Co}_x\text{O}_3$ with $x = \{0.125, 0.25\}$ [4,5] (Figures A2–A4); such U values also partially capture distinctive features concluded from hybrid calculations for STFC [34], and are used here to also calculate the oxygen-migration barriers and paths. For the purpose of validating our ferroelectric calculations with GGA+U, we performed additional calculations by using the screened hybrid Heyd–Scuseria–Ernzerhof (HSE06) functional [49] with $2 \times 2 \times 2$ and $4 \times 4 \times 4$ k -points grids, for a selected set of states, and results are presented in Appendix E.

The electric polarization was calculated by using the Berry phase approach [50]. In this work, we do not consider the ferroelectric response if the systems are metallic systems [51,52]. Instead, screening based on the formation energy of the defective structures is used to narrow the configurations to the more interesting insulating v_{O} states. The calculations involving the Berry phase theory were done with the implementation provided by VASP [50], and the quantum-of-polarization space analysis, which is discussed in section IV, was performed with homemade software. The pre- and post-processing of data required for this work were performed with VESTA [53], CrystalMaker[®] [54], and pymatgen-based programs [55].

$\text{SrTi}_{0.75}\text{Fe}_{0.125}\text{Co}_{0.125}\text{O}_{3-\delta}$ prototypes were modeled by using $2 \times 2 \times 2$ supercells, with the pair of Fe–Co ions aligned along [100], [110], and [111] directions, as shown in the upper panel of Figure 1a. Once the three configurations were analyzed, which is done by testing all the valence states admissible for the TM stoichiometry and the possible spin polarizations, v_{O} are created by removing one ($\delta = 0.125 \Rightarrow \delta_{01}$) or two ($\delta = 0.25 \Rightarrow \delta_{02}$) oxygen atoms out of the relaxed $\delta = 0 \Rightarrow \delta_0$ systems, and the resulting structures are grouped following a symmetry analysis of the configuration space with a tolerance of between 10^{-3} – 10^{-4} Å. For δ_{01} , such an analysis leads to seven nonequivalent O-deficient configurations for [100]

and [110] TM alignments. The [111] alignment has three configurations, all of them shown in Figure 1a. In the case of δ_{02} , there exists a total of 156 nonequivalent double-vacancy structures. For each configuration, we have again considered all the atomic valence states, which are reflected in several possible high and low Pauli states for the TM, as well as the possible combinations for the ferromagnetic (FM) or antiferromagnetic (AFM) Co–Fe exchange coupling. This FM/AFM notation that we have used is plausible in the sense that our DFT methodology uses periodic boundary conditions to construct the crystal out of the supercells in Figure 1; however, for nonuniform distributions of Fe and Co ions, these orderings would be just locally correct. Fe and Co magnetic moments generally differ in magnitude, such that in the AFM alignment the system has a finite magnetization (i.e., it is strictly speaking ferrimagnetic); nonetheless, we retain the notation AFM for sake of simplicity. The valences of the cations are such that we maintain a neutral supercell for a given oxygen deficiency, and charged defects are not considered because our calculations suggest spontaneous charging of the v_O is negligible, even for an excess or deficiency of electrons, in agreement with hybrid simulations [34]; therefore, a charge background is not used [56]. We initialized the systems with those combinations, and then relaxations without magnetic constraints were performed [5].

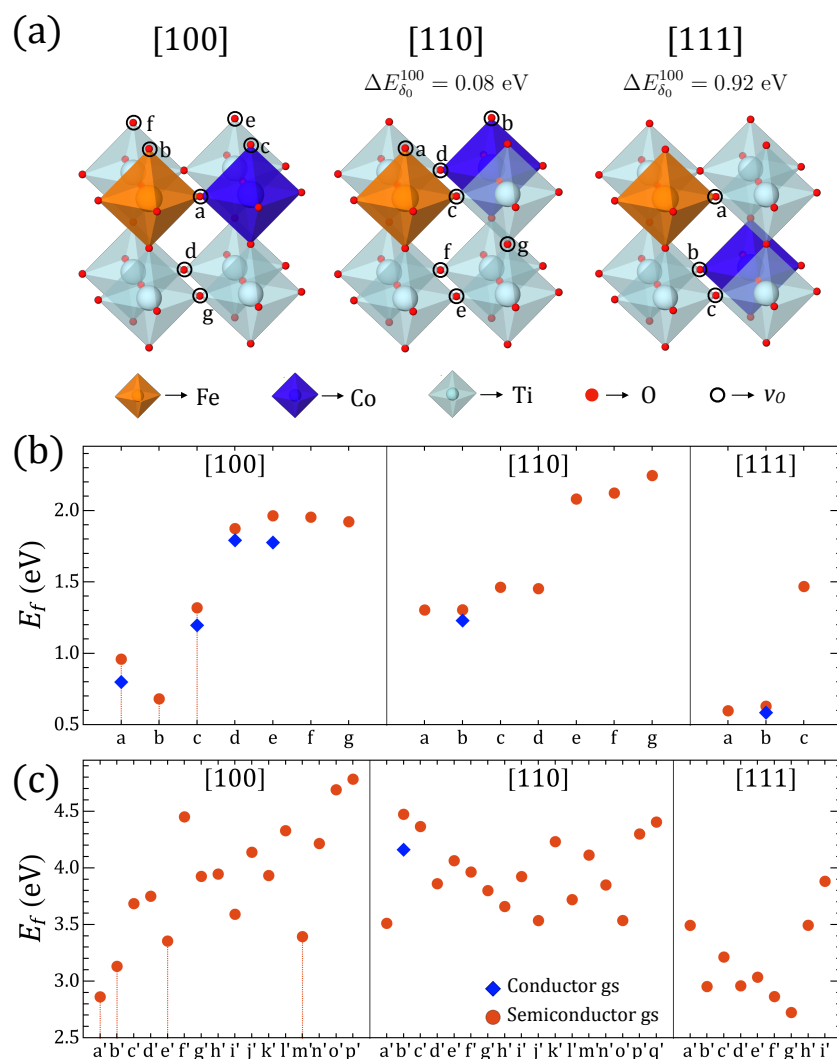


Figure 1. (a) Fe–Co arrangements in a $2 \times 2 \times 2$ perovskite cell and v_O positions for δ_{01} . $\Delta E_{\delta_0}^{100}$ = difference with [100] configuration. (b) Formation energies E_f for the ground state (GS) found for all v_O in the three Fe–Co configurations for δ_{01} , and (c) E_f for δ_{02} ; v_O positions are labeled with letters as defined in Figure A1 of the Appendix A. Solutions marked with vertical lines, a, b, c (δ_{01}), and a', b', e', and m' (δ_{02}) are used for subsequent analysis.

Although O deficiency is commonly observed in experiments, a path to use it to selectively enhance ferroic parameters is still unknown. The data obtained in this work provides insight into a general approach. We consider materials that favour large local magnetic moments, which implies states with at least one v_O coordinating either a Fe or Co cation, as this favors high-spin states [5,34] and therefore a larger magnetization per unit cell. This constraint narrowed our configurations down to 59 structures which are displayed in Figures 1 and A1. We then analyze their formation energies, remembering that although for STC and STF the [100], [110], and [111] alignments of the Co or Fe ions display energetically distinct states for the same magnetic saturation [4–6,34], and that for most cations the chemical potentials are equal to the DFT ground-state energies, for some elements at $T = 0$ the ground state (GS) is inadequate as a reference state and corrections to the energies should be made (e.g., to elements with structural phase transitions below room temperature (Ti, Na, Sn), diatomic gases (O), and elements subjected to +U corrections [57]). Moreover, different coordination numbers due to vacancy distributions are related to the ionic radii, which in turn can be related to various valence states; therefore, comparing the Equation (1) results is more appropriate than total energy comparisons. The expression for the formation energy E_f is

$$E_f = E_{v_O} - E_{\delta_0} + N_{v_O}\mu_O, \quad (1)$$

where E_{v_O} is the total energy of the defective crystal after relaxation, and E_{δ_0} is the total energy of the crystal corresponding to δ_0 . N_{v_O} is the number of removed oxygen atoms, and μ_O the chemical potential with respect to O_2 [58]. The energies obtained with Equation (1) are also corrected by using the fitted experimental enthalpies, as GGA/PBE calculations for O_2 tend to suffer from overbinding errors [59,60]. The resulting energies are presented in Figure 1 according to the respective orientations of the Fe–Co pairs i.e., along [100], [110], and [111] crystalline axes.

In what follows, we use the data in Figure 1 to evaluate the ferroic order parameters of STFC by using a representative set of states that are selected as described below. The ferroic order parameters are compared in terms of the oxygen deficiency δ , and for each δ an oxygen-migration analysis connecting the lowest-energy vacancy states is performed in search of those insights that lead us to further understand how to design a multiferroic perovskite by controlling its oxygen content.

3. Results

3.1. Representative Configurations

The results of the evaluation of Equation (1) for the remaining v_O ground states (GSs) described in the previous section are depicted in Figure 1 panel (b) for δ_{01} and panel (c) for δ_{02} . Although most of the GSs are semiconductors, there are few configurations which possess a slightly lower energy semi-metallic solution among the several possible initializations mentioned above. In those cases, we have shown both solutions for the sake of illustration, although the lowest energy solution for what turned out to be the most representative Fe–Co crystal arrangement is a semiconductor state in either δ_{01} or δ_{02} cases. Moreover, TM cations, such as the magnetic Fe and Co, are able to accommodate a wider range of spin states than their diamagnetic counterparts; therefore, any response of the valence states to oxygen content could also lead to hopping conductivity [61]. Mobile charges would screen out the electric polarization, limiting the ferroelectric response; therefore, we focus on the semiconductor states, which were also compared to the GSs from hybrid DFT calculations [34], and allow us to evaluate the electric polarization within the Berry phase approach.

Considering the results of Figure 1, a preference for the v_O to be coordinated by [100]- and [111]-oriented Fe–Co pairs is observed, as Ti–Ti coordinated vacancies tend to have significantly higher E_f . This is consistent with the preference for at least one O_5 uncompleted octahedral site hosting Co and Fe ions, reducing the number of δ_{02} configurations to be analysed. However, the total energy differences between configurations with [100]-oriented Co–Fe and the other two orientations for δ_{01} and δ_{02} deficiencies is

at least ~ 0.6 eV and ~ 0.7 eV, respectively, when comparing [100] and [110], with even larger differences for [111]. Moreover, the energy differences between Fe–Co pairs favor [100]-configurations by ~ 0.1 vs. [110] and ~ 0.9 eV vs. [111], as Figure 1a shows.

We comprehensively analyzed the magnetic/electric order parameters of the three lowest-energy GSs of O-deficient structures with the [100] Fe–Co arrangement and δ_{01} as pointed out in Figure 1 (vertical lines). In the case of the same cation arrangement for δ_{02} , we analyzed the three lowest GSs plus a fourth GS that is energetically closest to the other three states, as also depicted in Figure 1. The structural and magnetic properties of these perovskites are described in Table 1. The system relaxes to FM ordering in the global GS with spin gaps below ~ 20 meV of AFM orderings in P1 and P4/mmm symmetries for δ_{01} and δ_{02} , respectively. P1 has the lowest symmetry due to the v_O oriented perpendicular to the Fe–Co alignment, which is responsible for the larger unit cell (UC) volume with respect to P4/mmm. The Fe and Co ions are stable as high spin states for δ_{01} and δ_{02} , and the magnetic moment/UC slightly increases from $[100]_b$ to $[100]_{a'}$, as both Fe and Co are sandwiched by a vacancies in a' . The band gap also increases significantly for any δ_{02} compared to any δ_{01} solution. FM and AFM orderings compete among GS solutions depending on the number and location of v_O with respect to the Fe–Co pair. These results are in partial agreement with hybrid calculations [4,5,34].

Table 1. Semiconductor GSs: $[100]_{a,b,c}$ for δ_{01} , Figure 1a; and $[100]_{a',b',e',m'}$ for δ_{02} , Figure 1b. ΔE with respect to the lowest GS. The space group was obtained by using a tolerance of 0.05 Å.

Vacancy	a (Å)	b (Å)	c (Å)	Volume (Å ³)	μ_B/Fe	μ_B/Co	μ_B/UC	Order	ΔE (meV/f.u.)	E_{gap} (eV)	Space Group
$[100]_a$	8.01113	8.00104	8.00101	512.843	3.96	3.21	0.87	AFM	17.1	0.0	P4mm
$[100]_a$	8.03717	7.9533	8.01124	512.094	4.10	3.43	8.90	FM	37.1	0.39	Pmm2
$[100]_b$	8.03101	7.97895	8.03229	514.696	3.37	2.90	0.84	AFM	0.8	0.40	P1
$[100]_b$	8.03693	7.97111	8.03031	514.442	3.41	2.91	6.87	FM	0.	0.45	P1
$[100]_c$	8.00861	7.99924	8.03576	514.793	3.60	2.87	6.91	FM	66.8	0.0	Pm
$[100]_c$	7.9939	8.01455	8.02041	513.847	4.12	3.32	0.91	AFM	82.1	0.64	Pmm2
$[100]_{a'}$	7.93281	8.0405	8.04098	512.883	3.63	2.88	1.00	AFM	0.	1.20	P4/mmm
$[100]_{a'}$	7.92617	8.04598	8.04597	513.122	3.64	2.87	7.02	FM	20.2	1.14	P4/mmm
$[100]_{b'}$	8.08034	8.07529	7.97517	520.313	4.08	2.91	6.88	FM	33.7	1.56	P1
$[100]_{b'}$	8.10709	8.03554	8.00719	521.573	4.07	2.85	0.88	AFM	46.1	1.55	Pm
$[100]_{e'}$	7.96727	8.09836	8.04881	519.323	4.07	2.87	0.85	AFM	61.6	1.32	Pm
$[100]_{e'}$	7.96523	8.10383	8.04897	519.551	4.09	2.92	6.84	FM	64.8	1.35	P1
$[100]_{m'}$	8.03584	8.10503	7.9565	518.213	4.08	2.87	2.84	AFM	66.5	1.77	Pmm2
$[100]_{m'}$	8.04113	8.10629	7.95194	518.337	4.09	2.92	8.83	FM	73.1	1.73	Pmm2

E_f in our analysis is not significantly affected by magnetic interactions between vacancies and the periodic boundary conditions images as suggested by HSE calculations in STC and STFC [5,34] i.e., as we shall discuss later, v_O distributions of interest seem to promote ferroelectric states partially because of the tendency of the $\pi(\text{d-p})$ orbitals to localize into lower symmetry structures while the degeneracies are broken principally by breaking Hund's rules [62,63], as suggested by the predominance of high spin states. Oxygen-mediated phase separation and nonnegligible defect interactions have been observed in similar materials and have been associated with negative or negligible E_f [64]; the stoichiometry and defect configurations analysed here do not suggest the occurrence of that phenomena in STFC.

The rest of this paper is focused on the differences in electrical polarization between the structures illustrated in Figure 2. Global GSs, as well as higher energy solutions, are considered so that magnetization and structural changes can be compared more generally along with the electrical polarization behavior.

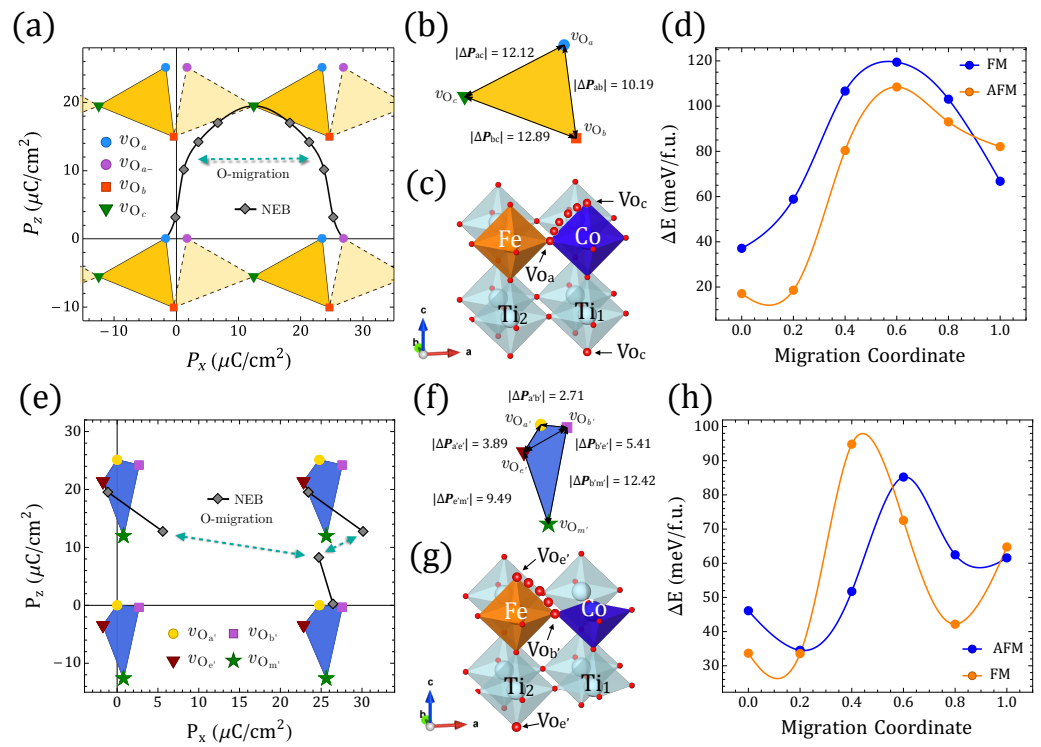


Figure 2. \mathbf{P}_Q differentiated polarization within the Berry phase approach. (a) $|\Delta\mathbf{P}|$ between δ_{01} gs in Table 1. Symmetrical x-axis \mathbf{P} for $[100]_a$ (dashed) is also shown. (b) The sides of the triangles represent the minimal $|\Delta\mathbf{P}|$ for the respective end-states in the inset frame; the $|\Delta\mathbf{P}|$ values are shown on each side. (c) STFC supercell with O migration between $[100]_a \Leftrightarrow [100]_c$ (\mathbf{P} fingerprint shown in (a)). (d) Energies relative to the δ_{01} gs along the $[100]_a \Leftrightarrow [100]_c$ migration for FM/AFM alignments ($[100]_a \Rightarrow$ migration coordinate 0.0; $[100]_c \Rightarrow$ migration coordinate 1.0). (e–h) The same information as presented in (a–d) but involving instead δ_{02} gs in Table 1 and the migration $[100]_{b'} \Leftrightarrow [100]_{e'}$ ($[100]_{b'} \Rightarrow$ migration coordinate 0.0; $[100]_{e'} \Rightarrow$ migration coordinate 1.0).

3.2. Electric Polarization and O Migration

The electric polarization order parameter is defined as follows:

$$\mathbf{P} = \mathbf{P}_{ion} + \mathbf{P}_{elec} \quad (2)$$

with \mathbf{P}_{ion} and \mathbf{P}_{elec} the ionic and electronic contributions respectively, which are given by

$$\mathbf{P}_{elec} = \sum_n^{occ} \frac{1}{V_{cell}} \sum_{j=1}^3 p_{nj} \mathbf{a}_j \quad (3)$$

$$\mathbf{P}_{ion} = \frac{e}{V_{cell}} \sum_i Z_i \boldsymbol{\theta}_i \quad (4)$$

where we have summed over the occupied n bands, and the ionic contribution is defined by the Z_i charges of the atomic nuclei and their positions $\boldsymbol{\theta}_i$ in the UC. The p_{nj} are the reduced polarizations, i.e., the components of the polarization along the primitive lattice vectors, which in terms of the reciprocal lattice vectors have the form

$$p_{nj} = \frac{V_{cell}}{2\pi} \mathbf{b}_j \cdot \mathbf{P}_n. \quad (5)$$

However, as the Bloch functions used to evaluate the Berry connections are not unique [65–68], two different sets of periodic functions follow the relation

$$\tilde{p}_{nj} = p_{nj} + em_j, \quad (6)$$

where m_j is an integer. Hence, the electric polarization can be expressed as

$$\tilde{\mathbf{P}}_n = \mathbf{P}_n + \frac{e}{V_{cell}} \sum_{j=1}^3 m_j \mathbf{a}_j = \mathbf{P}_n + \frac{e\mathbf{R}}{V_{cell}}, \quad (7)$$

with $\mathbf{R} = m_1 \mathbf{a}_1 + m_2 \mathbf{a}_2 + m_3 \mathbf{a}_3$ a lattice vector. This result implies that the polarization is well-defined just up to the modulus of the $e\mathbf{R}/V_{cell}$ quantity (i.e., all the points defined by Equation (7) are valid solutions to Equation (2)). The quantity separating two different polarization values is called the quantum of polarization \mathbf{P}_Q

$$\mathbf{P}_Q = e\mathbf{R}/V_{cell}. \quad (8)$$

This quantum is subject to the indeterminacy introduced by the freedom to choose the atomic base for a periodic lattice of point charges. Moreover, \mathbf{P} is invariant to unitary unit cell translations for which moving the origin of coordinates is not generally a way to resolve the multiple polarization values as would be the case if the total polarization was a well-defined basal property. This leaves us with a property that can be found from a lattice of polarization, the different components of which along the lattice vectors are expanded by \mathbf{P}_Q , such that $\mathbf{P} = \mathbf{P}_{ion} + \mathbf{P}_{elec} + \mathbf{P}_Q$. $\Delta\mathbf{P}$ is only determined within such a quantum uncertainty; hence, the process of resolving the polarization requires evaluation at intermediate steps connecting the end structures of interest; this will result in branches of polarization separated by quanta as displayed in Figure 2 [65–68]. Some of the processes that can be used to generate intermediate linking structures are ionic displacements, defect migration, applying strain, and/or inducing structural changes with pressure or external fields [65,66].

Let us discuss now the evaluation of $\Delta\mathbf{P}$ for the systems in Table 1. Figure 2a,e reveal the values of the electrical polarization lattices in STFC for δ_{01} and δ_{02} , correspondingly. In order to obtain the change in the polarization, which is the more meaningful quantity from an experimental point of view, we compared the lowest GS by using the lattice of polarization given by the different \mathbf{P}_Q solutions, and in that lattice the figures formed by joining the \mathbf{P} points associated with each defect configuration will have sides of magnitude equivalent to $|\Delta\mathbf{P}|$. Our first observation is very promising: Figure 2a for δ_{01} shows that O-deficient STFC perovskites can have sufficiently noncentrosymmetric polar structures to yield outstanding $|\Delta\mathbf{P}|$ values. Figure 2b enlarges the smallest possible changes in polarization, within $e\mathbf{R}/V$ uncertainty, which occurs when the system transitions from $[100]_a$ to $[100]_b$ (i.e., $10.19 \mu\text{C}/\text{cm}^2$); by comparing $[100]_c$ - $[100]_b$ or $[100]_a$ - $[100]_c$, we obtain $12.89 \mu\text{C}/\text{cm}^2$ and $12.12 \mu\text{C}/\text{cm}^2$, respectively. These values are in the range of the polarization of known ferroelectrics [1,2,69].

To resolve $|\Delta\mathbf{P}|$, we find the values of the polarization between the end points defining two different structures in Table 1. Those values connect two vertices that might be separated by different \mathbf{P}_Q , in which case $|\Delta\mathbf{P}|$ values would be larger than the ones mentioned above, and would capture features associated with electronic structure changes that differentiate those ground states. Structural deformation due to oxygen diffusion could lower the symmetry and lead to large lattice-parameter changes as in strained/pressure-induced ferroic transitions, and charge transfer and redistribution could be mediated by migrating oxygen [4,6,70]. Hence, we analyze the effects of adiabatic oxygen migration by following NEB-relaxed paths [71,72] between selected v_O sites. Figure 2 displays two representative migrations, and Figures A5–A10 contain additional examples.

Symmetry-equivalent v_O configurations lead to symmetric barriers, whereas migrations connecting energetically different configurations are represented by asymmetric barriers as seen in Figures 2 and A5–A10, which resemble, for example, oxygen diffusion along different O_5 -defined NaBiTiO_3 planes [73]. In our case, for instance, symmetric $[100]_c$ v_O have the z - y plane defining $\Delta\mathbf{P}$ as P_x does not change in that rotation, but the local magnetic moments do not change either because neither Fe nor Co coordinations are being modified (Figure A7). The migration barriers for symmetric cases are in gen-

eral comparable or even larger than nonsymmetric ones, and in the process of tuning the ferroelectric and/or magnetic order parameters, energetically different v_O are most likely to be involved in an oxygen-driven structural accommodation, which leaves us with the migrations $[100]_a$ to/from $[100]_c$ or $[100]_b$ if we restrict for sake of comparison to ΔE approximated to the separation between the lowest and the second-lowest GS. We display in Figure 2a the continuous polarization footprint of a system in which an oxygen moves from the Fe–O–Co position to the v_O in $[100]_c$ and back to the v_O in $[100]_a$ along the path illustrated in Figure 2c. Moreover, in Figure A8 the results for migration between a and b are shown.

In the migration from $[100]_a$ to $[100]_c$ the semiconducting character of the system is preserved throughout the intermediate migration states independently of the spin polarization, and it has a y -reflection symmetry and thence provides $P_y = 0$ -centered solutions for the polarization. The FM path requires slightly more energy than the AFM one although it is lower in the vicinity of the $[100]_c$ end point Figure 2d, which means it would require around the spin-gap energy difference to maintain the material as a semiconductor throughout the whole path. The magnetization/UC would decrease because of the change in magnetic order rather than due to a decrease in the local magnetic moments observed in the FM path (Figure A5), which is also related to the steepest decrease of the energy band gap in this last path as TM orbital occupancy is slightly increased; such magnetization is nonetheless of considerable magnitude $\sim 1 \mu_B$. The electric polarization on the other hand is now not restricted to the closest values within the \mathbf{P} lattice, such that $|\Delta\mathbf{P}|$ for $[100]_a$ - $[100]_c$ vacancy switching would reach $\sim 24 \mu\text{C}/\text{cm}^2$.

Figure 2e presents the values of the electric polarization components as well as the $|\Delta\mathbf{P}|$ values between the δ_{02} structures in the same way that Figure 2a does for δ_{01} but using instead the four δ_{02} structures in Table 1. We can also see the electric polarization fingerprint for the adiabatic O migration of the Fe–O–Ti oxygen perpendicular to the Fe–Co line in $[100]_{b'}$ to the Fe– v_O –Co in $[100]_{b'}$, leading to $[100]_{e'}$, as Figure 2g illustrates. As we compare figures (b) and (f), it is clear that lowest energy GS for δ_{02} provides a smaller $|\Delta\mathbf{P}|$ than those obtained with δ_{01} . We have to take into account an energetically expensive fourth GS $[100]_{m'}$ in order to reach similar polarization values with two vacancies (e.g., differences between the first two GS configurations for δ_{01} and δ_{02} are $10.19 \mu\text{C}/\text{cm}^2$ and $2.71 \mu\text{C}/\text{cm}^2$, respectively); this is a persistent trend among O-deficient perovskites in Figure 1. This leads to the observation that connected polar end structures for δ_{01} yield larger $|\Delta\mathbf{P}|$ than those obtained for δ_{02} .

A second observation is that crystals with such increased δ yield $|\Delta\mathbf{P}|$ differences that are more sensitive to the v_O symmetry and are consistently larger when, among the three energetically lowest v_O , the two compared δ_{02} configurations share a c vacancy. In contrast, sharing no vacancies or sharing a vacancies leads to lower changes of polarization. The inclusion of g vacancies always increases the changes of the polarization but, unlike the result for the lowest three GSs, it will favor the duplicity of the a defects. The energy barrier for δ_{02} between $[100]_{b'}$ and $[100]_{e'}$ also shows an energy difference between FM and AFM polarizations, which favors the AFM e' polarization throughout the migration path in terms of energy, but the spin gap is again relevant in the vicinity of the Fe–O–Ti oxygen position. A third general observation that we can extract from Figures 2, A5 and A6 is that for δ_{01} it is possible to find an oxygen migration linking two distinct configurations in Table 1 (or their symmetrical representations), which could generate a finite $\Delta\mathbf{P}$ through a continuous polarization footprint connecting the end states. For δ_{02} , however, such a polarization footprint presents a nonmonotonic path due to polarization jumps of magnitude comparable to the differences in polarization between the GS configurations for δ_{01} and δ_{02} within the first \mathbf{P}_Q . Whereas for δ_{01} , uncompleted paths could be found (e.g., when some of the intermediate states turned out to be metallic), in the δ_{02} case not just all the end states are semiconductors, but they remained as such when disturbed by the vacancy relocation. Therefore, the polarization can always be defined but not always be fully resolved. A change in the branch \mathbf{P}_Q separating the available end solutions of the electric polarization

should always consider at least the closest one as is evident, for instance, in Figure 2e, where the migration path suggests two different $|\Delta\mathbf{P}|$ that are different from the one in Figure 2f (i.e., $|\Delta\mathbf{P}| \sim 36 \mu\text{C}/\text{cm}^2$ and $|\Delta\mathbf{P}| \sim 21 \mu\text{C}/\text{cm}^2$, as seen in Figure 3 at $\delta = 0.25$). In the following section, we will discuss these jumps of polarization along with several other features of the magnetic/electric response of our oxygen-deficient perovskites.

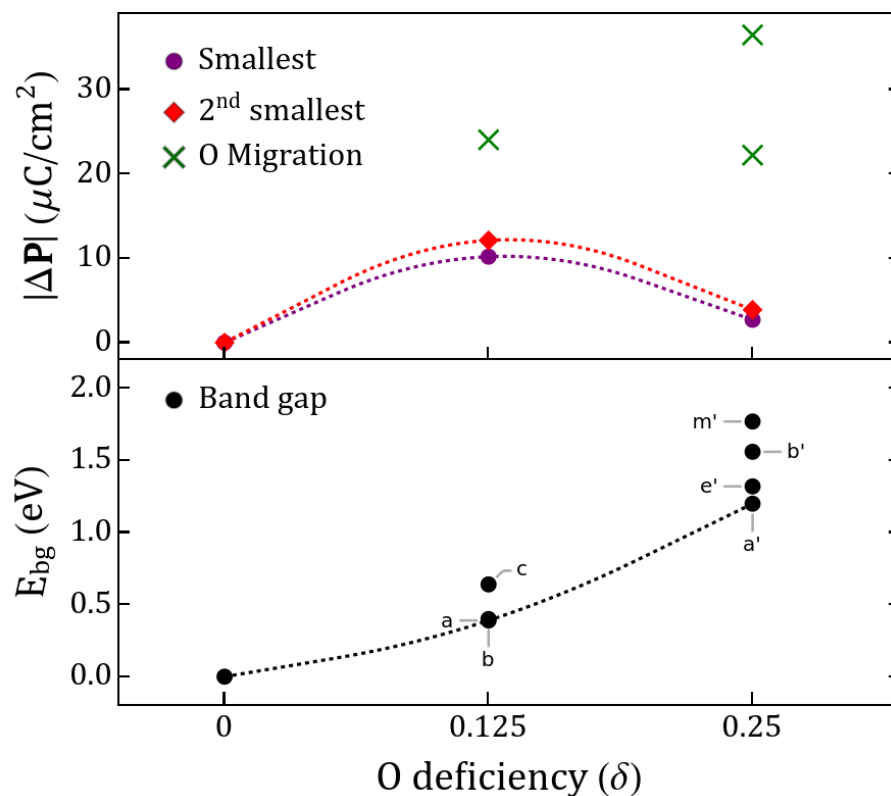


Figure 3. (Top panel) Polarization changes $|\Delta\mathbf{P}|$ between studied configurations and (bottom panel) band gap. The lowest two $|\Delta\mathbf{P}|$ at each δ (dashed lines) are shown. $|\Delta\mathbf{P}|$ obtained from migrations shown in Figure 2a,b are marked with crosses. Band gaps shown for δ_{01} and δ_{02} correspond to the lowest-energy semiconductor states of Table 1.

The results so far show that the O-deficient STFC is indeed electrically polarized, as well as magnetic, and can display a significant change of electric polarization by tuning the oxygen vacancy content and/or transporting oxygen while maintaining the crystal among the stable solid solutions along paths with various energy barriers depending on the magnetic configuration of the end states. Furthermore, we have shown that FM or AFM ground states have a different saturation magnetization that provides the material with two field-tunable order parameters. The relation between the magnetic and ferroelectric behavior according to the role of TM cations (Co/Fe), migration paths and the structural and electronic trends will be discussed in the next section along with an intuitive picture of the effect of varying oxygen pressure during growth to obtain a specific multiferroic response of the material.

4. Discussion

The polarization changes have been discussed in terms of oxygen diffusion, which may be controlled electrochemically (e.g., by ionic liquid gating or oxygen pumping), or it may be driven by temperature fluctuations or strain effects. This provides the possibility of direct control over the polarizability of such materials post-growth, as well as via the oxygen pressure during growth. In Figure 3 we show that although the centrosymmetric stoichiometric solutions do not predict a switchable polarization, increasing the deficiency δ of the perovskite yields polarization changes $|\Delta\mathbf{P}|$ that are larger for δ_{01} and decrease

for δ_{02} . However, in both cases a migration mechanism can improve upon such a value, providing us with at least twice the initial response for one v_O and up to ~ 4 –6 times for two v_O . The largest $|\Delta\mathbf{P}|$ attainable, according to our calculations, likely requires vacancy migration. This mechanism has been widely studied in solid perovskite fuel cells, perovskite-based capacitors, solid electrolytes and all-oxide electronics [74,75]; however, its use in multiferroics as a mechanism to assist ferroic-order is unexplored.

Considering the GS, Figure 4 suggests the magnetization follows a similar behavior as the changes of the electric polarization when δ increases. However, if migration occurs, for instance for δ_{01} between a and c , the magnetization would decrease considerably while the electric polarization switches. On the other hand, when oxygen migrates between a and b sites, the magnetization will slightly decrease while the change of the polarization cannot be determined as the system becomes metallic at intermediate points of the migration. For the migration in Figure 2e,f at $\delta = 0.25$, we will have an inverse change in $|\Delta\mathbf{P}|$, increasing when relaxing from e' to b' , while the magnetization/UC decreases. This magnetization behavior qualitatively replicates the experimental magnetization trends of STF [4]. The maximization of both polarization and magnetic moment in some of the cases is intriguing considering the effect of 3D occupancy in perovskites, i.e., partly filled 3D orbitals promote magnetism but disfavor FE [1,2].

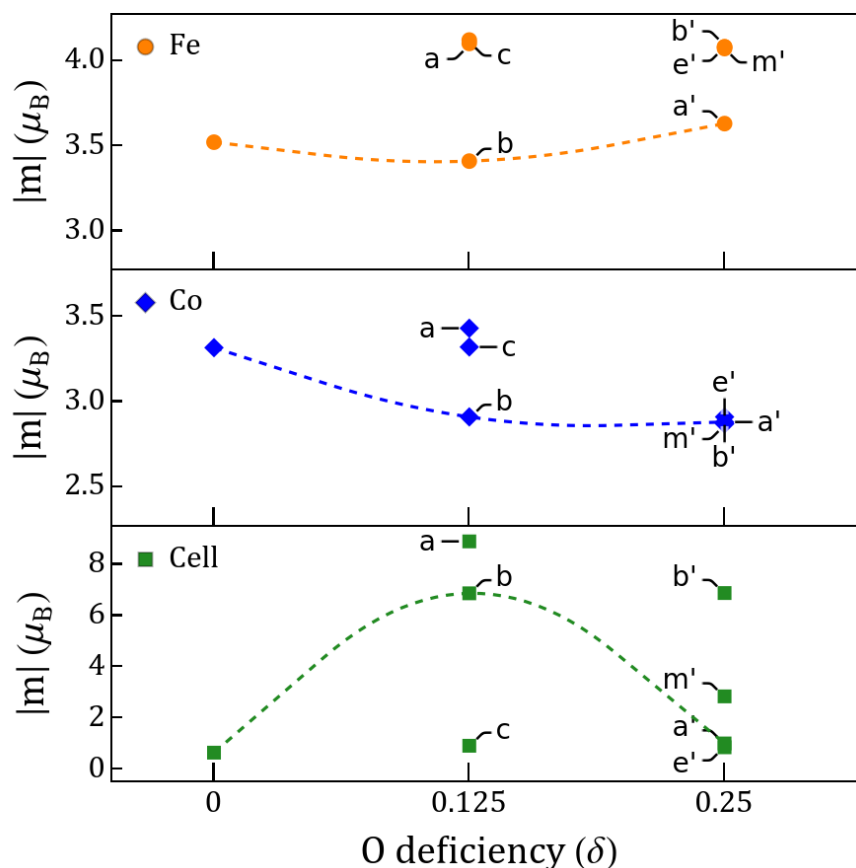


Figure 4. Fe/Co and cell magnetic moment vs. δ . Values shown for δ_{01} and δ_{02} correspond to the lowest-energy semiconductor states of Table 1.

Let us now analyze the roles of Co and Fe during oxygen migration. Comparing vacancies a and c for δ_{01} , Figure 4 shows that the largest change of the magnetic order parameter is not due to a change in the electronic occupancy of the TMs as the vacancy moves between Fe–O₆/Fe–O₅ and Co–O₅, but to the magnetic switching between the two energetically close GSs. The Co has a very small change of its magnetic moment compared to δ_0 solutions, whereas Fe has increased more appreciably for δ_{01} , being then responsible for any effective saturation magnetization of the c solution. Figure 5 displays the differences

between the electronic occupancy of Co/Fe and the cation polarization, which is driven by the rotation of the v_O in the Co–O₅ with respect to the Fe–Co line as Figure 6 also illustrates. In Figure 7, we can see that such vacancy interchange will modify the total and d-orbital charges of the Co even though it remains in an uncompleted oxygen octahedral coordination, due to the larger electronegativity of Co with respect to Fe. In addition, the smaller changes for Fe still give rise to a slightly larger increase of the local magnetic moment, which is a sign of an intrinsic charge reorganization among the hybridized orbitals of the Fe–O–Co bonding.

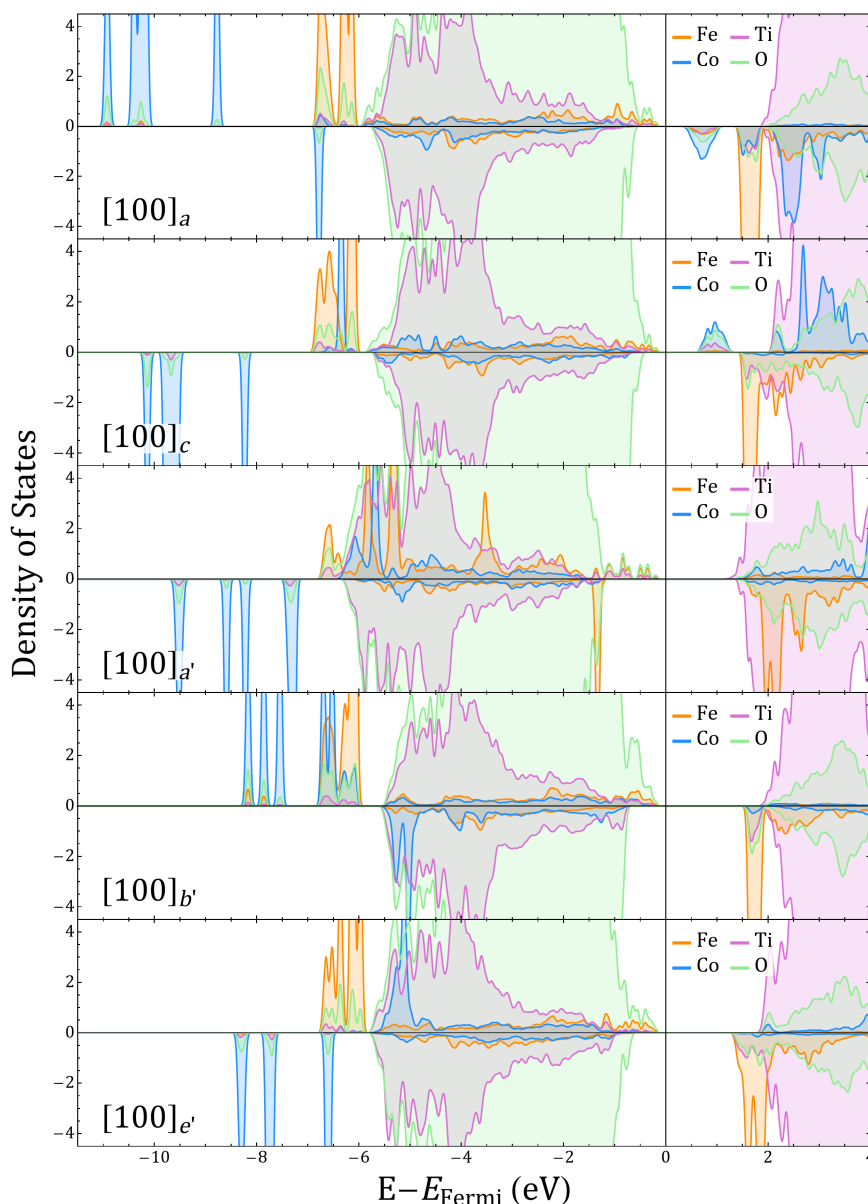
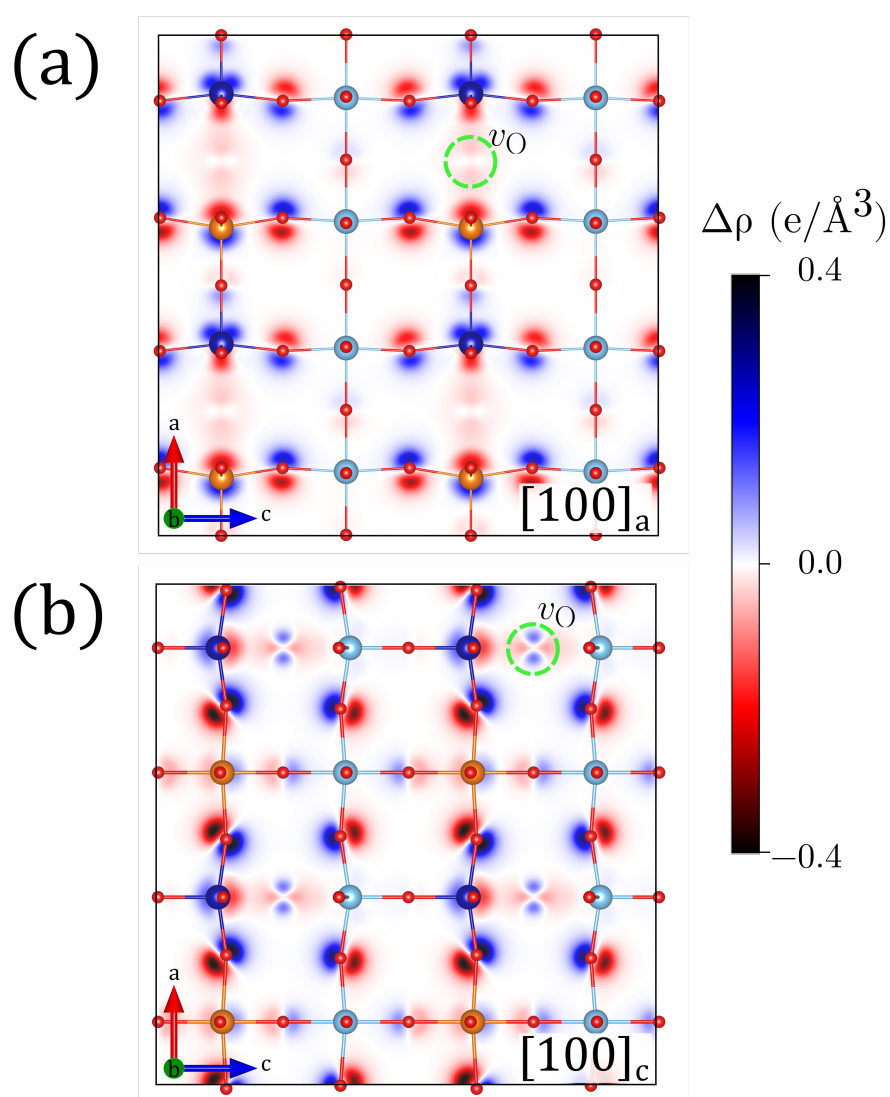


Figure 5. Fe, Co, Ti, and O projected density of states (DOS) for $[100]_{a,c}$ and $[100]_{a',b',e'}$ corresponding to δ_{01} and δ_{02} , respectively.

Figure 6 shows density charge differences of a and c for δ_{01} with respect to the nonoxygen-deficient system. These representations, which are calculated for defective structures with the same symmetry as in Table 1, provide a simple but powerful insight about the origin of the electric polarization in the perovskites. The resulting structures are noncentrosymmetric and have off-centered Co and Fe cations as well as Ti ions. The uncompleted Fe/Co–O₅ octahedra present local bending with respect to the plane perpendicular to the Fe– v_O –Co and Ti– v_O –Co directions that is reflected in tetrahedral lattice distortions.

The symmetry of the charge density suggests that the creation of the oxygen vacancy has promoted a subtle charge redistribution that is more evident in the case of Co cations as they present a larger change of local charge. Fe and Co coordinations also show distinct characteristics beyond the ionic radii changes that are triggered by the 3d-2p hybridization of the TM at the Fe-O₅ and Co-O₅ centers, as also suggested by the projected density of states in Figures 5 and A11. One of the signatures of the Fe and Co behavior can be seen in Figure 5. For δ_{01} Co, hybridization defines the acceptor-like states delimiting the band gap whereas half-filled Fe states form the Fermi limit of the valence band. For δ_{02} , the additional electrons partially occupy the acceptor states, increasing the gap and proving the propensity of Co to fill 3D orbitals under variations of charge, whereas Fe orbitals tend to reach high-spin states so that the closest empty state has always opposed polarization to the majority populated states. These features are useful ingredients for the generation of a material whose ferroic degrees of freedom do not exclude each other.



Charge density difference ($\Delta\rho$)

Figure 6. Projected charge density difference $\Delta\rho = \rho(\delta_{01}) - \rho(\delta_0) + \rho(O_{\text{Removed}})$ (in a 2×2 unit cells projection), with ρ the respective charge densities, for $[100]_a$ (a) and $[100]_c$ (b) configurations. Charge accumulation/depletion (positive/negative $\Delta\rho$) is represented by using blue/red colors. A green-dashed circle has been used to highlight the v_O local position (one out of four is displayed).

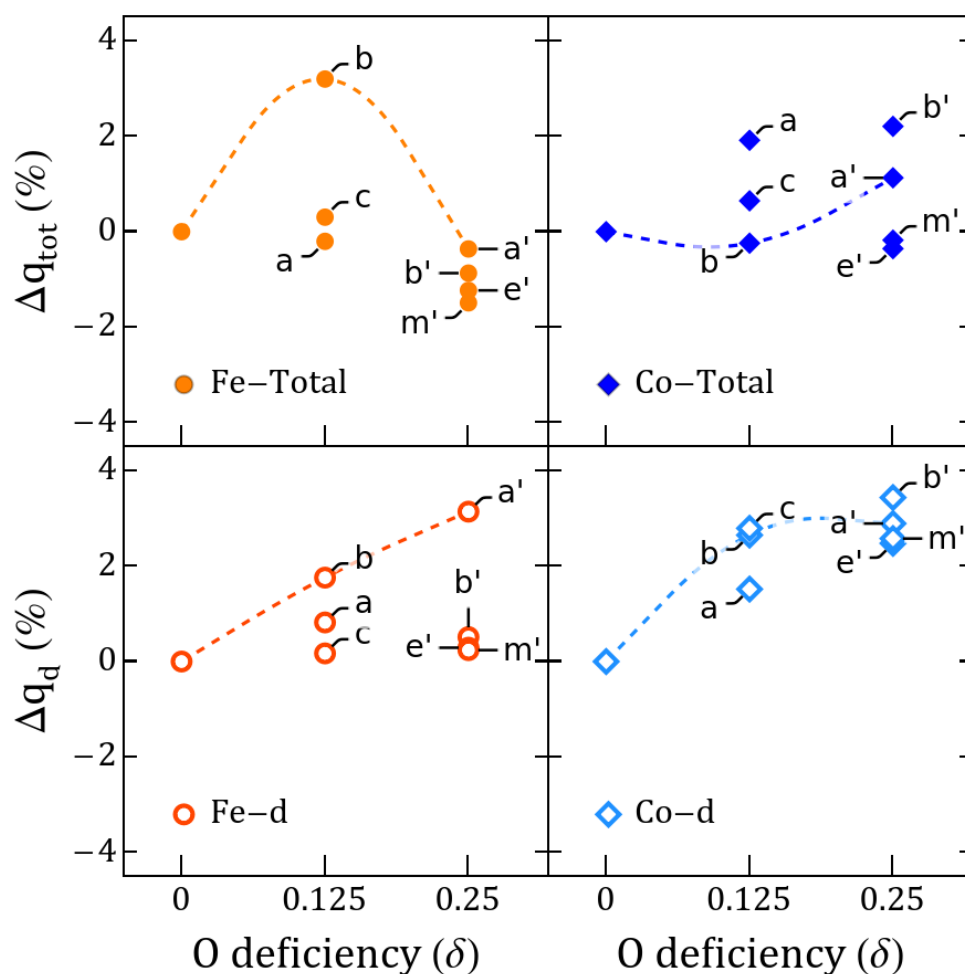


Figure 7. Total and d-orbital Fe/Co charge variation vs. δ with respect to δ_0 perovskites. Values shown for δ_{01} and δ_{02} correspond to the lowest-energy semiconductor states of Table 1.

With the introduction of a second vacancy, which for the sake of comparison is either a , b , or c , we know that the minimal electric polarization changes tend to decrease. b' could maintain an FM magnetization, whereas e' presents an AFM coupling with nonzero magnetization as the Co and Fe local moments change. Figure 7 shows that the additional c - v_O mimics what happens with $\delta = 0.125$, and Fe decreases its charge even further, whereas Co does the opposite for b' . This is consistent with the fact that we have Co–O₄ and Fe–O₅ octahedra (b and c are the second and third GSs for δ_{01} as well as b' and e' for δ_{02} , respectively, these last differing in the vacancy switching $a - b$). The change in Co d-occupancy are favored, but, unexpectedly, the change for Fe is negligible. Comparing c to e' , Fe–O₆ converts to a Fe–O₅ without a Fe– $n v_O$ –Co, which for δ_{01} favors a change in d-occupancy of Co. Compared with Figure 4 and the projected density of states in Figure A11, it is clear then that the Fe/Co $t_{2g}e_g$ electron population is no longer defining the saturation magnetization alone. The previously magnetically neutral Ti are able now to play a role by contributing with a magnetization equivalent to one electron, as seen in Figure A6, where the magnetization originates on the O₅-coordinated Ti₁ for Co– v_O –Ti in $[100]_{b'}$ and Ti₂ for Fe– v_O –Ti in $[100]_{e'}$.

Ti₂ for instance, as seen in Figures 2 and A6 for migrations between b' and e' , passes from zero to a finite $\sim 1\mu_B$ halfway along the migration path; Ti₁ behaves in the opposite manner. This happens when the Co coordination passes from O₄ to O₅ whereas the Fe coordination remains O₅. In this last configuration, a Co–O–Ti₁ 3d-2p hybridization turns Ti₁ off with that additional Co charge as Figures 7 and 5 show. When oxygen migrates to form a , the Ti octahedra can intuitively be thought of as having a charge transfer process

in which Ti_2 now has a similar hybridization to that described for $Fe-O-Ti_2$, with the Ti now in an uncompleted $Ti-O_5$. This magnetization process of Ti ions through hybridised orbitals represents a process in which an electron is given and received due to the different electronegativities and electronic valences, as well as to the local defect topology with respect to the neighboring TM cations. It differs from what happens in vacancy-induced magnetism in $SrTiO_{3-\delta}$ [7], as in that case nonfilled 3d-Ti orbitals can locally define the magnetization. The $Ti_{1,2}$ magnetic activation in b' and e' is then due to a superexchange-like mechanism between those ions that is dominated by the Co and Fe electronic environmental response to the v_O .

Figure 8 gives a pictorial description of the charge transfer due to the relocation of the vacancies, which is equivalent to the change in the TM octahedral coordinations. In the case of the migration in Figure 2 the Fe and Ti_1 remain in 5 coordination but Co and Ti_2 change from 4 to 5 and 6 to 5 coordination, respectively. A Ti coordination changed by 1 means that an effective electron charge loss or gain, which means a $\mp 1\mu_B$ change in Ti magnetization. On the other hand, the change in the local magnetic TM will change the TM valence spin state. An effective $\pm 1\mu_B$ variation in the Ti will result from the hybridizations, as the covalent character of the Co/Fe-O- $Ti_{1,2}$ persists. The initial polarization of the Ti ions with respect to the magnetic cations follows the magnetic description here and in references [4,5,34], which puts the $Ti_{1,2}$ ions with a different polarization with respect to Co-Fe FM coupling and the opposite of that for AFM coupling. The magnetic solutions for the crystal images in between the end states will simply switch, as can be seen in Figure A5 for all the δ_{02} migrations. This behavior just described is common among all the δ_{02} systems we handled in this investigation.

Figures A5–A10 show that migration barriers in STFC range between ~ 40 – 130 meV/f.u., with the lowest values obtained for migrations involving “excited” vacancies coordinating Ti ions. Comparatively, some of the previously calculated barriers for STO are around ~ 50 meV/f.u. [76]. Our energy barriers indicate the possible costs of an oxygen mobility process. They are measured with respect to the global GS in Table 1 and connect end states that can have slightly different symmetries. Features such as the small well-like steps separating the large barrier from the stable GS are attributed mostly to the relaxation of the $O_{5,4}$ uncompleted octahedra, whose bending with respect to the Co/Fe- v_O line changes during the migration. O_5 undergoes an initial rigid rotation before the planes perpendicular to the (Fe/Co)- v_O bend. This asymmetric energy landscape resembles the trapping effect in Gd-doped CeO_2 [77] which, however, can be tuned through oxygen vacancy migration. Pronounced features, which reach negative energy in a few cases, represent the instability of the intermediate states when a conductor–semiconductor transition is possible, as Figure A8 shows. Although the final path of the oxygen could lead the ions into otherwise interoctahedral space, as displayed by the z -(x , y) solutions for the NEB coordinates in Figure A7, this is not really an interstitial diffusion phenomenon, as observed in electrolytes under strain [78] or in promotion of TM shifting/diffusion through v_O migration in bulk $LiNiO_2$ [79]. In this last case, and in our STFC, there is always a spin polarization solution that keeps the system semiconducting. In general, oxygen migration between $O_{4,5,6}$ sites depends on the pathway and the coordinating A(B) ions for the end- v_O . We have three different B ions stabilized in different spin states, so we expect our systems to mimic a variety of features for the migration barriers as described for O_2 diffusion in $NaBiTiO_3$ [73]. The changes in ferroic order parameters still depend upon the full relaxed GS.

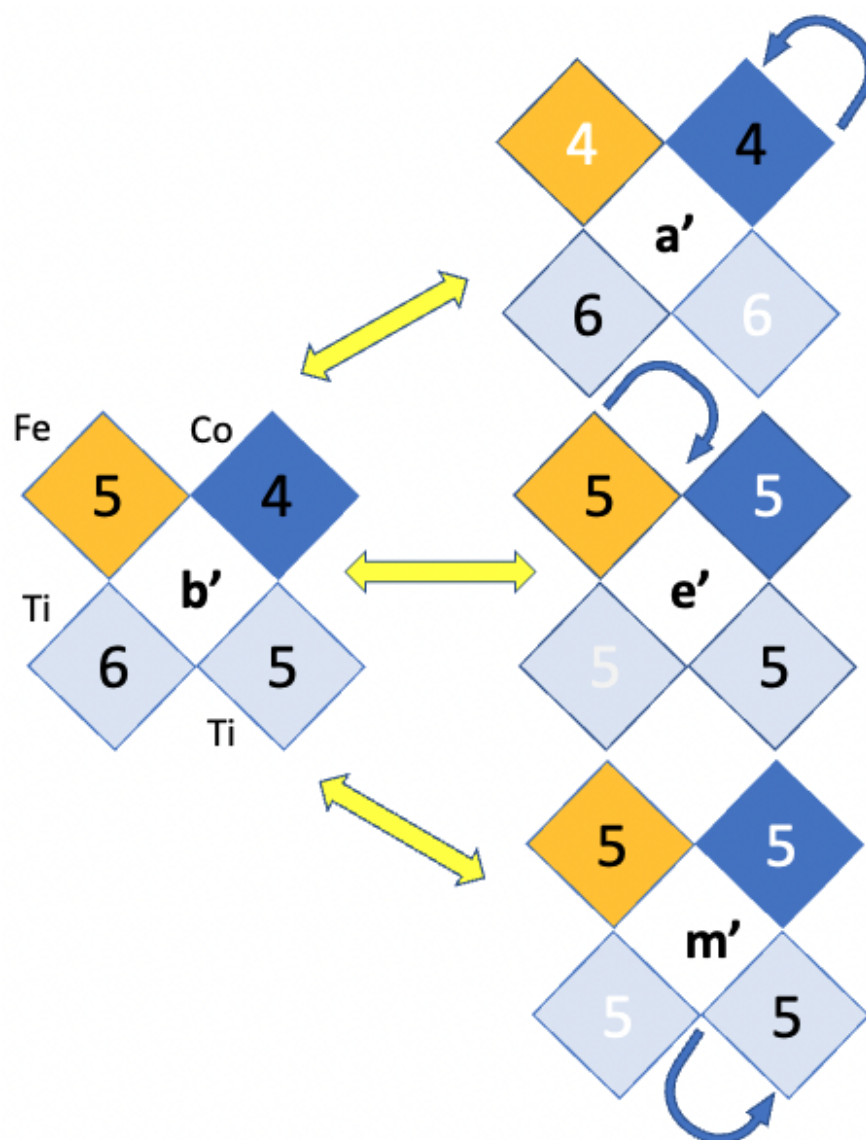


Figure 8. Coordinations of the Ti, Co, and $Ti_{1,2}$ ions as the migrations connecting b' with a' , e' , and m' occur. Arrows point out the vertex between which the oxygen move starting in this case, e.g., from b' . Black numbers represents O coordinations that do not change from b' to any other configuration whereas white ones have changed by 1.

Lattice distortions in Figure 6 and Table 1 suggest that $|\Delta P|$ for δ_{02} configurations could be enhanced by lattice strain, which is useful if we were to use strain mechanisms to tune the migration barriers while conserving specific symmetries for the defective end structures [78]. The structural effect of vacancies can itself produce or suppress polar structures, e.g., $[100]_a$ has a $P4mm$ structure without inversion symmetry along the Fe–Co direction whereas $[100]_c$ has a $Pmm2$ orthorhombic structure. They both represent a finite change of the electric polarization as seen in Figure 2. In the GS case for δ_{02} , the inclusion of a second v_O in O–Fe– v_O –Co reestablishes the inversion symmetry and as a consequence the polarization decreases. Nonetheless, any $|\Delta P|$ still requires a nonzero band gap. Although δ_{02} systems are semiconductors, the migration paths in Figures 2, A9 and A10 seem to be unable to completely resolve $|\Delta P|$, even when such semiconductor behavior remains in the intermediate structures. This is because of the jumps in the polarization fingerprint, which follow the charge transfer that separates the two end states, as Figure 5 and supplementary figures illustrate. A denser grid of intermediate structures would still have some jumps in the path as charge is redistributed into ions that are in generally not symmetrically

equivalent, which are responsible for the largest part of the polarization change. The magnetization could be used to narrow the structural region of imminent electronic transfer by using, for instance, a climbing point technique, but this is beyond the scope of this work.

In our search for the STFC electric order parameter, we have used a semi-local functional that is adapted to the TM nature of the solid solution through the $+U$, which, in turn, we fixed to a plausible value after a systematic analysis of the GS and experimental properties of several STO-based magnetic solutions. Nonetheless, it is pertinent to check the robustness of the electric polarization behavior in Figure 2 when we modify $+U$. To do this, we have chosen the δ_{01} configurations, as they display similar changes of electric polarization for a given δ . Then, we tune $+U$ of Co because among the TM studied here, Co is the species associated with more possible U values. Figure A15 displays the triangles of electric polarization changes as calculated for several U_{Co} . We have kept $U_{Co} > 5$ eV, because lower values can render the system conductive, as suggested in Figure A14. Figure A15a shows that the electric polarization changes do not depend, importantly, on the U value for Co within that range, independently of the vacancy location. Figure A15b displays the same calculations, but in this case using both an HSE functional constrained to the same conditions as in Figure A15a, and a total HSE relaxation, which is then also constrained magnetically. These last figures show a decent agreement between the GGA+ U predictions and the HSE ones. That is, the magnitude of the changes of the polarization are similar, and the major differences do not seem to come primarily from the improvements that HSE does by capturing the spin occupancy more precisely, but from its ability to capture slightly better some of those subtle structural changes created by the v_O , which converge differently than the magnetism. A study of the possible magneto-electric coupling in these tentative multiferroic materials would require more sophisticated methods that could provide us with more precise U values for every vacancy distribution, for instance, by using cRPA calculations [80]. On the other hand, the use of oxygen deficiency as a trigger to multiferroic behavior requires us to classify accurately the metallic or semiconductor characteristics of systems that relax to energetically close GSs corresponding to different spin states. Although HSE and similar hybrid methods are useful in that respect, new methodologies such as occupation matrix control (OMC) [81] could offer an opportunity to deal with these oxygen-deficient perovskites improving upon hybrid methods with respect to computational times, screening parametrization and spin initializations.

The concepts discussed here to modulate the order parameters by tuning the oxygen deficiency as well as promoting oxygen mobility in O-deficient structures should be capable of experimental demonstration. Engineering of O-deficient TM-based magnets/ferroelectrics is now within reach. Stable three-state nonvolatile memory devices were realized by combining both ferroelectricity and oxygen vacancy migration in Pt/BTO/STO, where oxygen vacancies modify the switching properties [82]. Combined in situ scanning probe and transmission electron microscopy has been used to study the field-induced migration of oxygen vacancies in thin films of PrCaMnO₃. The oxygen vacancies in the material have been imaged in situ and are found to migrate under an external electric field [83]. Measurements of thermally stimulated and pyroelectric currents were performed in STO single crystals subjected to an electric field. A dielectric-to-pyroelectric phase transition in an originally centrosymmetric crystal structure with an inherent dipole moment is found, which is induced by oxygen migration [84]. Moreover, changes in oxygen content are achievable, e.g., by ionic liquid gating, so one has a path to modulating the properties in real time [85]. For instance, it has been recently shown that a redox-driven reversible topotactic transformation in epitaxial SrFe_{0.8}Co_{0.2}O_{3- δ} thin films can be achieved at room temperature and at atmospheric pressure. This transformation triggers changes in electronic structures as well. Reversible redox reactions and/or associated changes at low temperature and under atmospheric pressure are particularly valuable to develop a cathode for solid-oxide fuel cells [86].

5. Conclusions

We demonstrated that STFC is a magnetic semiconductor capable of sustaining electric polar structures for a range of TM orderings and O deficiencies. Variations of δ and O migration are effective mechanisms by which to tune magnetic and electric polarization changes and therefore engineer perovskites by using O deficiency and cation arrangement. The Fe and Co TM contribute differently to the order parameters according to their electronegativity, radii, and spin valences, which allows us to design a variety of vacancy densities and cation and vacancy distributions such that both magnetic and ferroelectric orderings can be enhanced.

The preferred ground states of STFC consist of layered perovskites with sheets of linearly organized $O_{4,5,6}$ -coordinated Fe–Co pairs, separated by Ti ions, and sandwiched with layers of O_5 -coordinated Ti, which provides a first suggestion for the engineering of a STFC-based multiferroic. The model suggests that v_O are not uniformly spread all over the crystal but they stabilize at the Fe–Co octahedra, resulting in a layered STFC in which the magnetic TM are locally undercoordinated in contrast to the Ti layers that are mostly not defective. The Co,Fe- v_O defects are the source of the crystal symmetry distortions, off-centering of cations and bending of the oxygen octahedra.

Oxygen deficiency of one v_O/UC yielded the largest values for the changes of the magnetic and electric parameters between different arrangements, although there are several stabilized structures that in the worst case scenario would always display a small but finite saturation magnetization, whereas the polarization changes are very similar among those structures. On the other hand, O deficiency of two v_O/UC usually provides smaller electric polarization changes as well as smaller saturation magnetization, but there are several stabilized structures with increased magnetization, and Ti can also provide a second source of magnetization.

Oxygen migration for $\delta = 0.125$ yields $|\Delta P| > \sim 10 \mu C/cm^2$ due to quantum-of-polarization differences between $\delta = 0.125$ structures. Increasing the deficiency to $\delta = 0.25$ yields $|\Delta P|$ the O migration of which resolved polarization for $\delta = 0.25$ is $> \sim 3 \mu C/cm^2$. These predicted values of electric polarization changes are large compared to TM-substituted STO multiferroics, motivating experimental synthesis and demonstration.

The results have been presented in the form of an intuitive set of rules for STFC to be multiferroic, but these rules are expected to be a particular case of a broader set for magnetic oxides based on the interplay between (Co/Fe)- v_O defects, TM-cation coordination, and topological vacancy disorder. The manipulation of electronic properties according to such rules could facilitate applications such as nonvolatile magnetoelectric memory or logic, or phase-change materials driven by oxygen content.

Author Contributions: Conceptualization, E.A.C.E., S.P.O., C.A.R. and J.M.F.; methodology, E.A.C.E., S.P.O. and J.M.F.; software, E.A.C.E. and J.M.F.; validation, E.A.C.E., S.P.O., C.A.R. and J.M.F.; formal analysis, E.A.C.E., S.P.O., C.A.R. and J.M.F.; investigation, E.A.C.E., S.P.O., C.A.R. and J.M.F.; resources, E.A.C.E. and J.M.F.; data curation, E.A.C.E. and J.M.F.; writing—original draft preparation, E.A.C.E., S.P.O., C.A.R. and J.M.F.; writing—review and editing, E.A.C.E., S.P.O., C.A.R. and J.M.F.; visualization, E.A.C.E.; supervision, S.P.O., C.A.R. and J.M.F. All authors have read and agreed to the published version of the manuscript.

Funding: This research was funded by Agencia Nacional de Investigación y Desarrollo: FONDECYT Regular 1221301; DGIIE-USM: PI_LIR_2021_100; National Science Foundation: DMR 1419807; National Science Foundation: DMR 2132623; United States Department of Energy: DE-AC02-05-CH11231; Materials Project program KC23MP.

Institutional Review Board Statement: Not applicable.

Informed Consent Statement: Not applicable.

Data Availability Statement: Not applicable.

Acknowledgments: J. M. Florez thanks project PI_LIR_2021_100 from DGIIE-USM and FONDECYT Regular 1221301; E. A. Cortés Estay thanks DGIIE-USM Master scholarship and PIIC-031. S. P. Ong acknowledges support from the Materials Project, funded by the U.S. Department of Energy, Office of Science, Office of Basic Energy Sciences, Materials Sciences and Engineering Division under contract no. DE-AC02-05-CH11231: Materials Project program KC23MP. C. A. Ross acknowledges support from NSF awards DMR 1419807 and 2132623.

Conflicts of Interest: The authors declare no conflict of interest.

Abbreviations

The following abbreviations are used in this manuscript:

STFC	$\text{SrTi}_{1-x-y}\text{Fe}_x\text{Co}_y\text{O}_{3-\delta}$
STF	$\text{SrTi}_{1-x}\text{Fe}_x\text{O}_{3-\delta}$
STC	$\text{SrTi}_{1-y}\text{Co}_y\text{O}_{3-\delta}$
STO	SrTiO_3
TM	Transition Metal
FE	Ferroelectric
FM	Ferromagnetic
AFM	Antiferromagnetic
DFT	Density Functional Theory
PAW	Projector-augmented-wave
GGA	Generalized Gradient Approximation
GGA+U	Generalized Gradient Approximation with Hubbard-like correction
PBE	Perdew-Burke-Ernzerhof
HSE	Heyd-Scuseria-Ernzerhof
NEB	Nudged Elastic Band

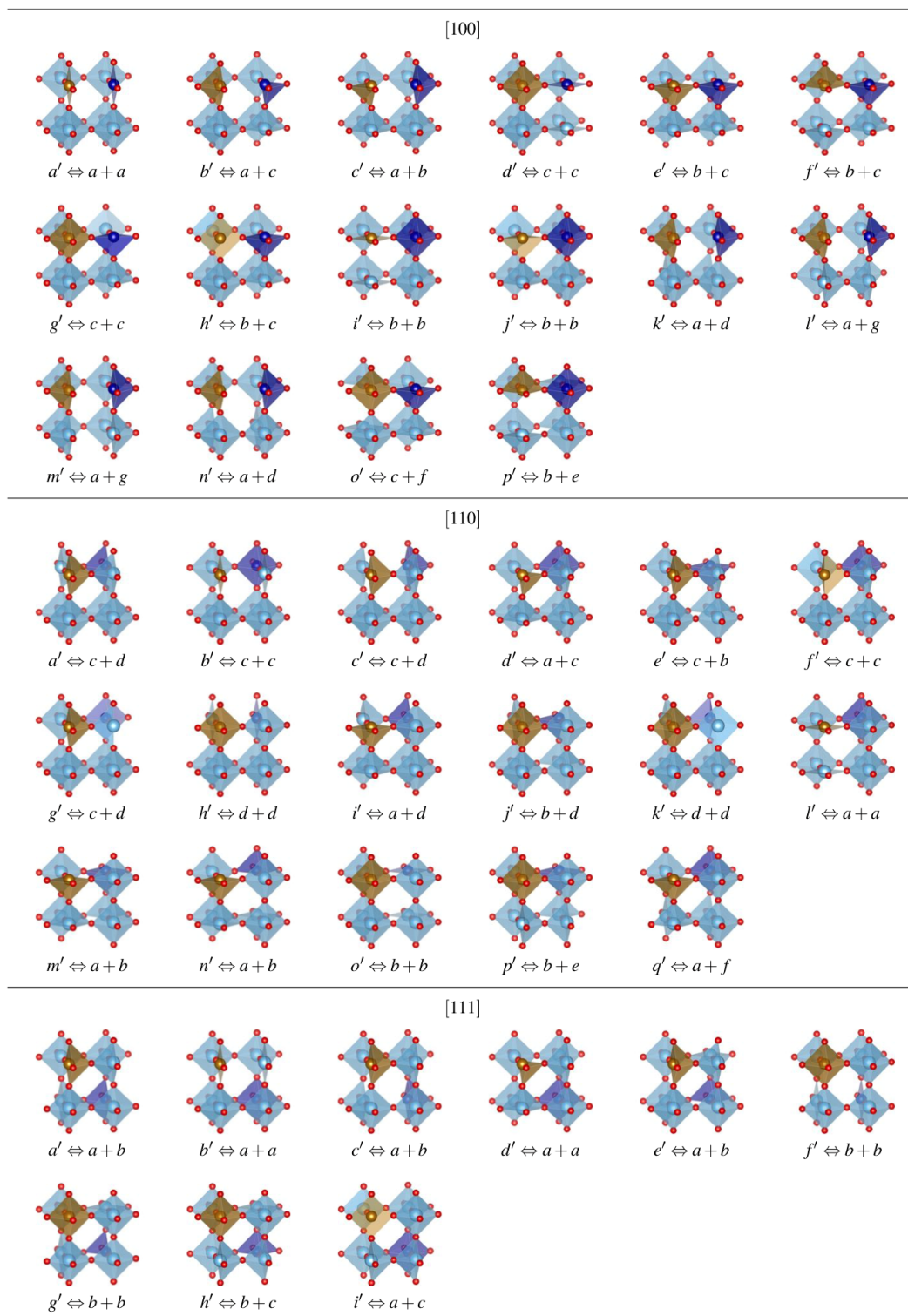
Appendix A. Configurations of Oxygen Vacancies for δ_{02} 

Figure A1. Configurations of oxygen vacancies for δ_{02} systems in main text Figure 1. For each Fe–Co orientation considered in this work, we labeled the different δ_{02} combinations in terms of the δ_{01} vacancies displayed in Figure 1.

Appendix B. GGA+U: Selection of Hubbard +U Parameters

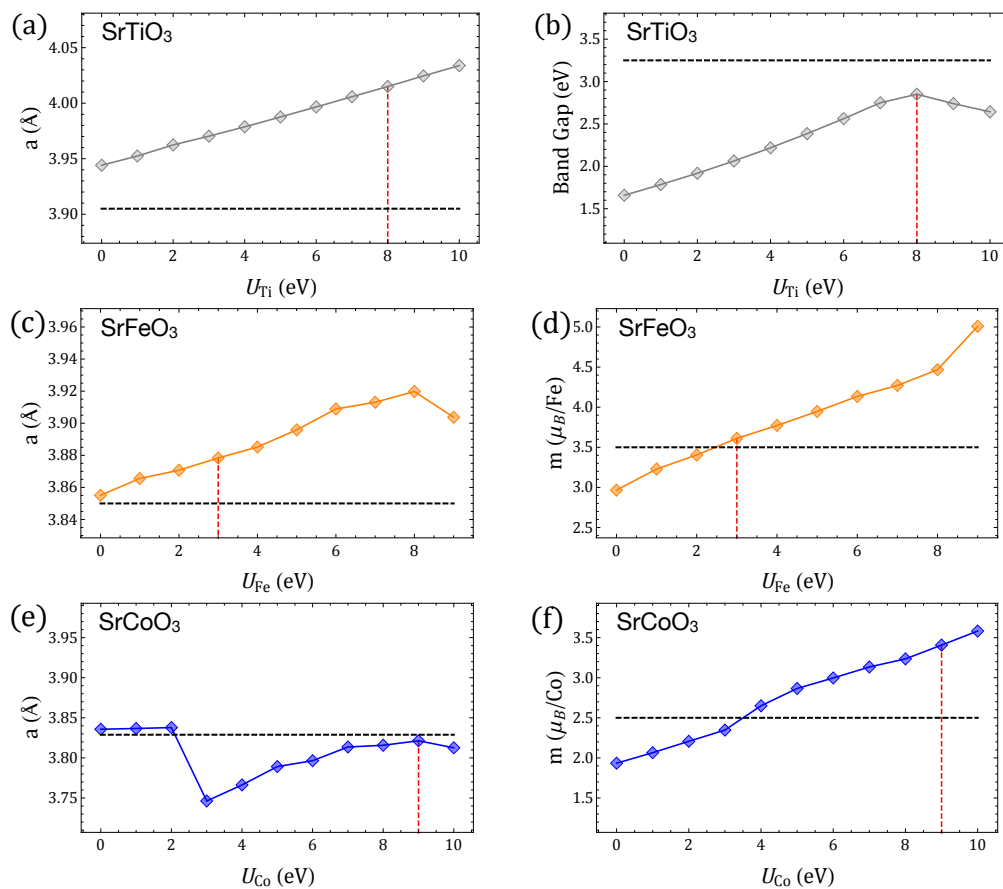


Figure A2. Properties of SrTiO₃, SrFeO₃ and SrCoO₃ perovskites calculated with GGA+U by using different Hubbard parameters for Ti, Fe, and Co. (a,b) Lattice parameter and band gap of SrTiO₃. (c–f) Lattice parameter and magnetic moment per Fe/Co ion of SrFeO₃ and SrCoO₃, respectively. Horizontal lines indicate the respective experimental values (from Refs. for SrTiO₃ [7], SrFeO₃ [87,88], SrCoO₃ [89]) whereas vertical lines indicate the U values chosen for this work.

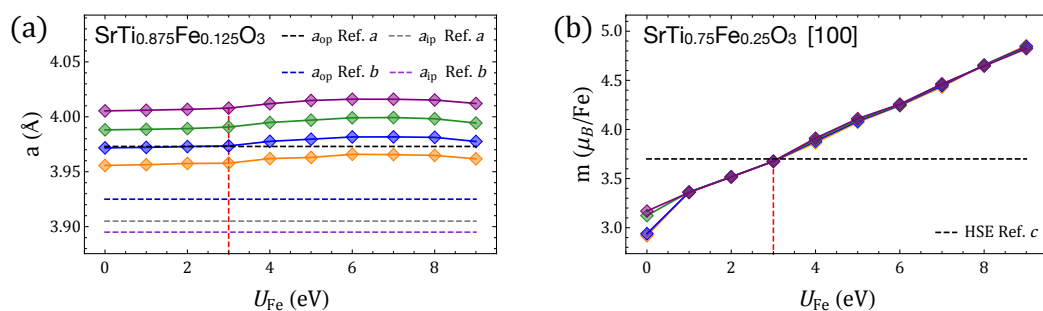


Figure A3. Properties of SrTi_{1-x}Fe_xO₃ perovskites ($x = \{0.125, 0.25\}$) calculated with GGA+U by using different Hubbard parameters for Ti and Fe. U_{Ti} takes values of 2, 4, 6, and 8 eV, represented by orange, blue, green, and purple diamonds, respectively. (a) Lattice parameter of SrTi_{0.875}Fe_{0.125}O₃ compared with experimental parameters for $x = 0.13$ (from Refs. a [90] and b [38]). (b) Magnetic moment per Fe ion for $x = 0.25$ compared with HSE results (Ref. c [4]).

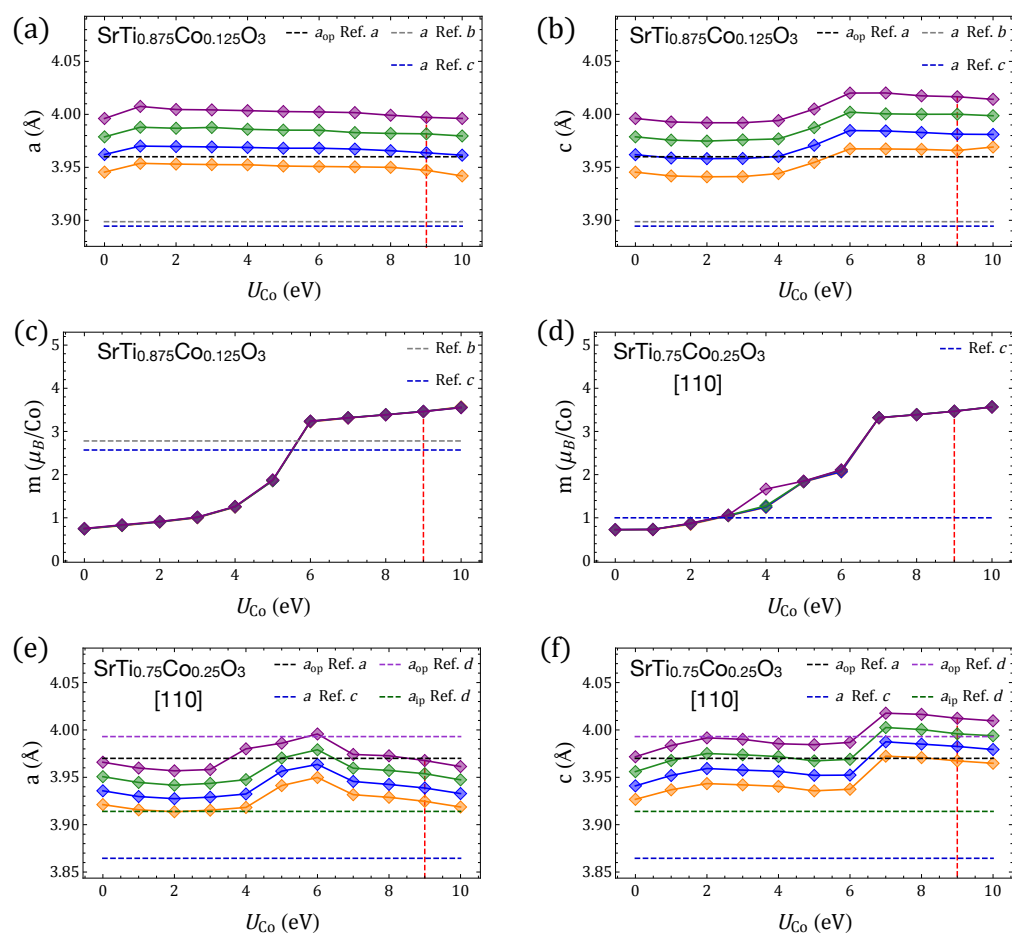


Figure A4. Properties of $\text{SrTi}_{1-x}\text{Co}_x\text{O}_3$ perovskites ($x = \{0.125, 0.25\}$) calculated with GGA+U by using different Hubbard parameters for Ti and Co. U_{Ti} takes values of 2, 4, 6, and 8 eV, represented by orange, blue, green, and purple diamonds, respectively. (a,b) Lattice parameters of $\text{SrTi}_{0.875}\text{Co}_{0.125}\text{O}_3$ compared with experimental parameters for $x = 0.14$ (from Refs. a [91] and b [92]) and HSE results (Ref. c [5]). (c,d) Magnetic moment per Co ion for $x = 0.125$ and $x = 0.25$. (e,f) Lattice parameters for $x = 0.25$ and [110]-aligned Co–Co, compared with experimental values for $x = 0.23$ (Refs. a and d [90]) and HSE calculations for $x = 0.25$ (Ref. c).

Appendix C. Oxygen-Vacancy Migration

In this section we present complementary information associated with the oxygen migrations shown in Figure 2 of the article main text as well as the results for two additional migration paths for δ_{01} systems. In all cases, the intermediate structural images representing the v_{O} migration are obtained through: (i) a linear interpolation, between the end structures, of the atomic coordinates and lattice vectors; (ii) a relaxation of such interpolation by using the nudged elastic band method (NEB). Depending on the end states magnetic ordering for δ_{01} and δ_{02} respectively, which are detailed in Table 1 of the article, the migration images were annotated FM or AFM.

Appendix C.1. Migration Path between δ_{01} vacancies in Figure 2: $[100]_a$ and $[100]_c$

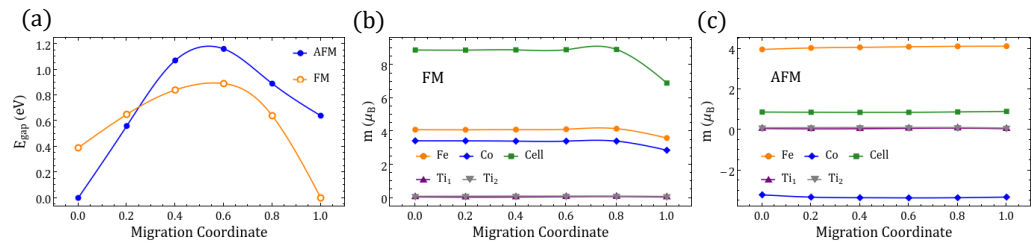


Figure A5. (a) Band gap E_{gap} along the migration path between $[100]_a$ (migration coordinate 0.0) and $[100]_c$ (migration coordinate 1.0) for FM and AFM NEB-relaxed structures. (b,c) Magnetic moment “m” of the TM labeled in Figure 2 of the main text, and of the whole perovskite supercell for the relaxed FM and AFM migration paths. End-state values are associated with the GS reported in Table 1.

Appendix C.2. Migration Path between δ_{02} vacancies in Figure 2: $[100]_{b'}$ and $[100]_{e'}$

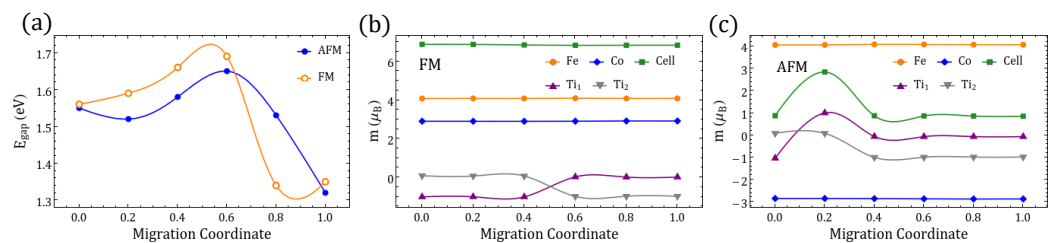


Figure A6. (a) Band gap E_{gap} along the migration path between $[100]_{b'}$ (migration coordinate 0.0) and $[100]_{e'}$ (migration coordinate 1.0) for FM and AFM NEB-relaxed structures. (b,c) Magnetic moment “m” of the TM labeled in Figure 2 of the main text, and of the whole perovskite supercell for the relaxed FM and AFM migration paths. End-state values are associated with the GS reported in Table 1.

Appendix C.3. Other Migration Paths for δ_{01}

Appendix C.3.1. Migration Connecting Symmetry-Equivalent Vacancies: The Case of $[100]_c$

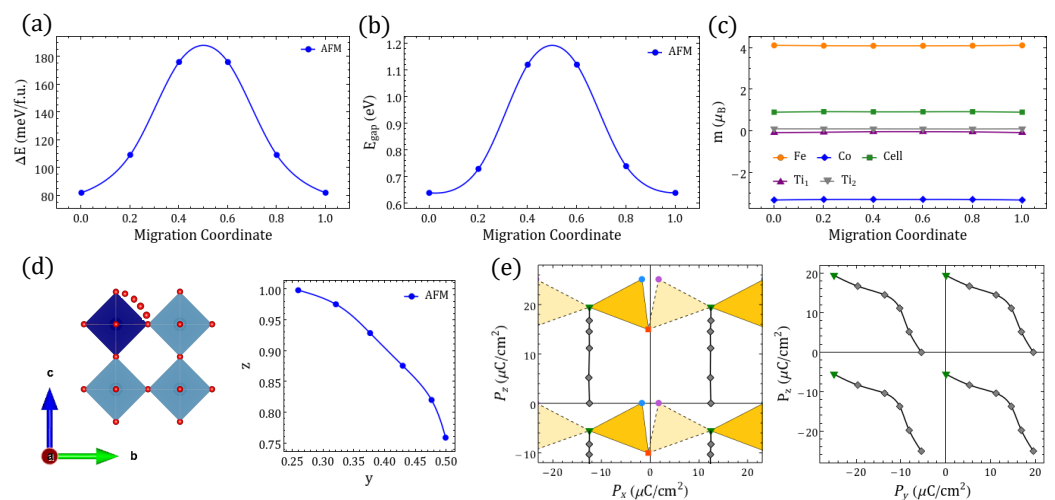


Figure A7. (a) Energy relative to the δ_{01} gs, (b) band gap E_{gap} and (c) magnetic moments “m” along the migration path between $[100]_c$ (migration coordinate 0.0) and a symmetrically equivalent structure (migration coordinate 1.0). (d) Oxygen-migration path in which Co– v_O –Ti switches from the c direction to the b direction, and the corresponding relaxed fractional position of the migrating oxygen. (e) Electric polarization lattices along NEB-relaxed paths.

Appendix C.3.2. Migration Connecting Nonequivalent Vacancies: The Case of $[100]_a$ and $[100]_b$

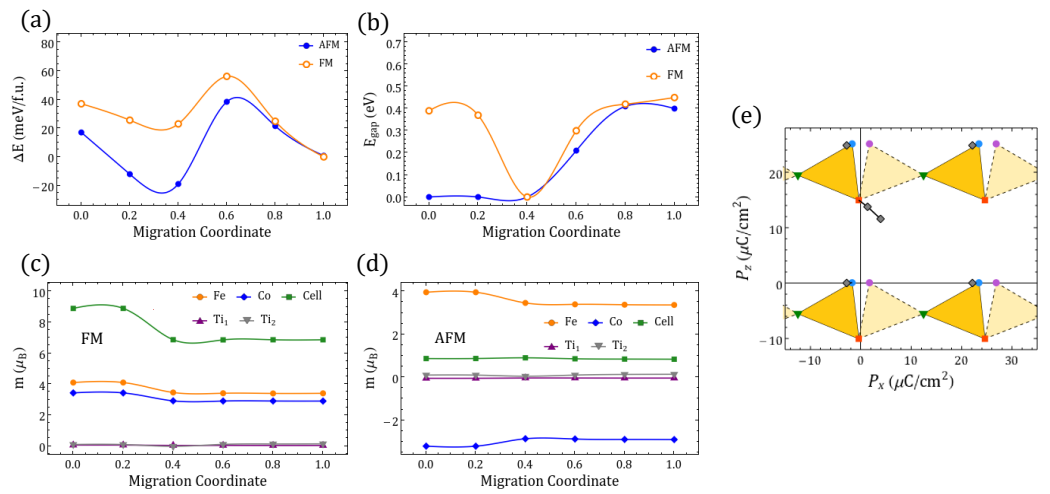


Figure A8. (a) Energy relative to the δ_{01} gs, (b) band gap E_{gap} and (c,d) magnetic moments “m” along the migration path between $[100]_a$ (migration coordinate 0.0) and $[100]_b$ (migration coordinate 1.0), for AFM and FM NEB-relaxed structures. (e) Electric polarization lattices corresponding to the FM NEB-relaxed path.

Appendix C.4. Other Migration Paths for δ_{02}

Appendix C.4.1. Migration Path between δ_{02} Vacancies: $[100]_{b'}$ and $[100]_{m'}$

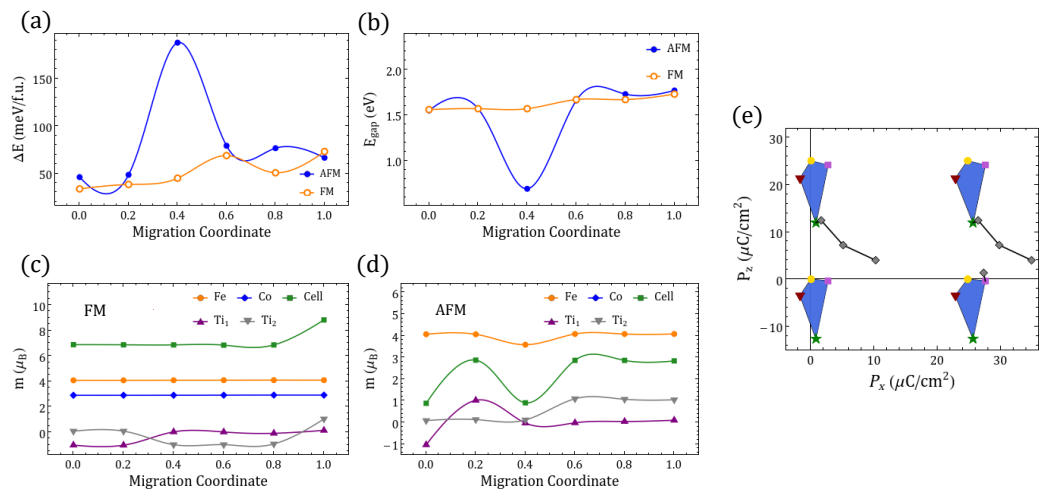


Figure A9. (a) Energy relative to the δ_{02} gs, (b) band gap E_{gap} and (c,d) magnetic moments “m” along the migration path between $[100]_{b'}$ (migration coordinate 0.0) and $[100]_{m'}$ (migration coordinate 1.0), for AFM and FM NEB-relaxed structures. (e) Electric polarization lattices corresponding to the FM NEB-relaxed path.

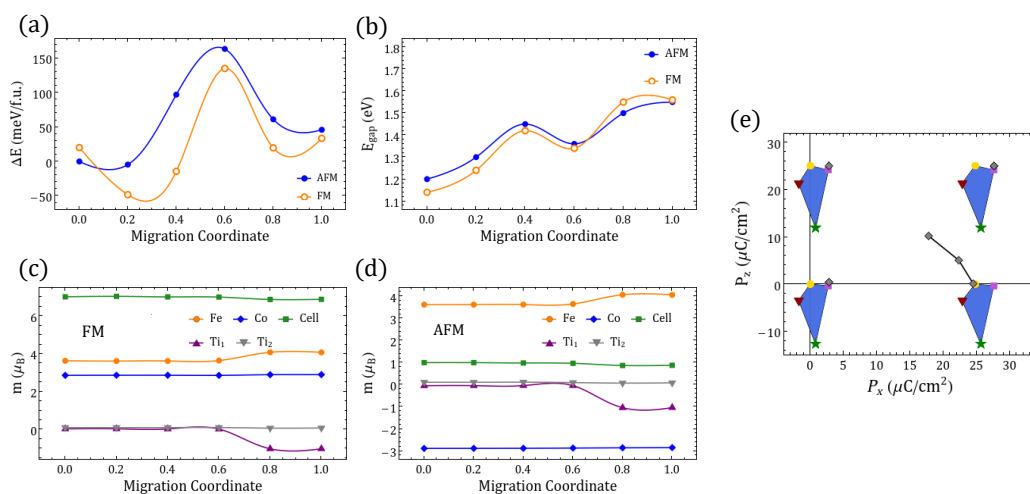
Appendix C.4.2. Migration Path between δ_{02} Vacancies: $[100]_{a'}$ and $[100]_{b'}$ 

Figure A10. (a) Energy relative to the δ_{02} gs, (b) band gap E_{gap} and (c,d) magnetic moments “ m ” along the migration path between $[100]_{a'}$ (migration coordinate 0.0) and $[100]_{b'}$ (migration coordinate 1.0), for AFM and FM NEB-relaxed structures. (e) Electric polarization lattices corresponding to the FM NEB-relaxed path.

Appendix D. Projected Density of States

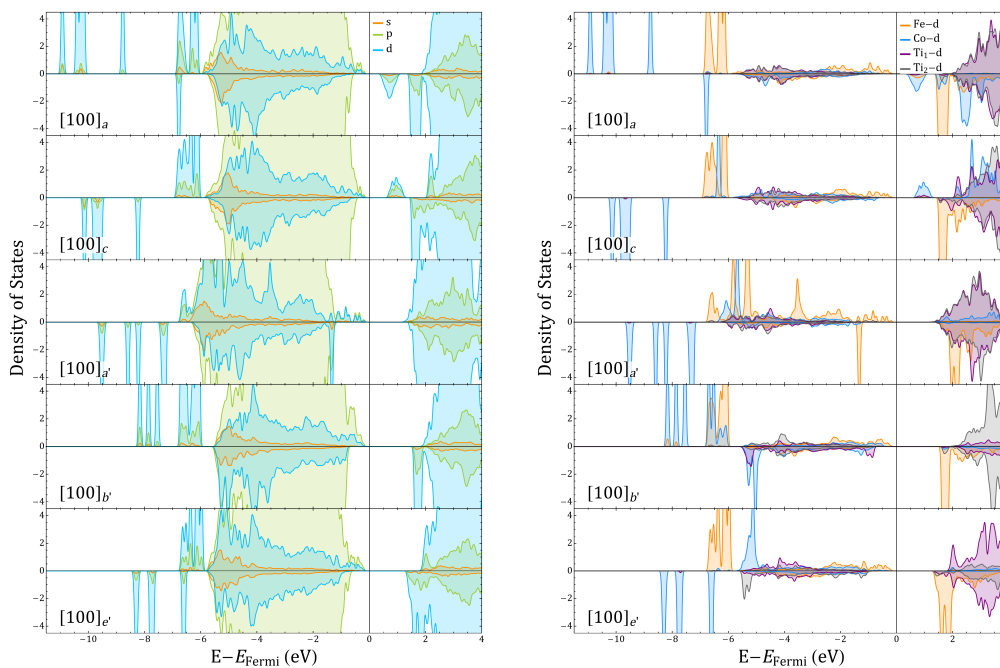


Figure A11. spd -decomposed density of states (left panel) and Fe, Co, Ti_1 , and Ti_2 d -orbital projected density of states (right panel) for $[100]_{a,c}$ and $[100]_{a',b',e'}$ vacancies corresponding to δ_{01} and δ_{02} , respectively.

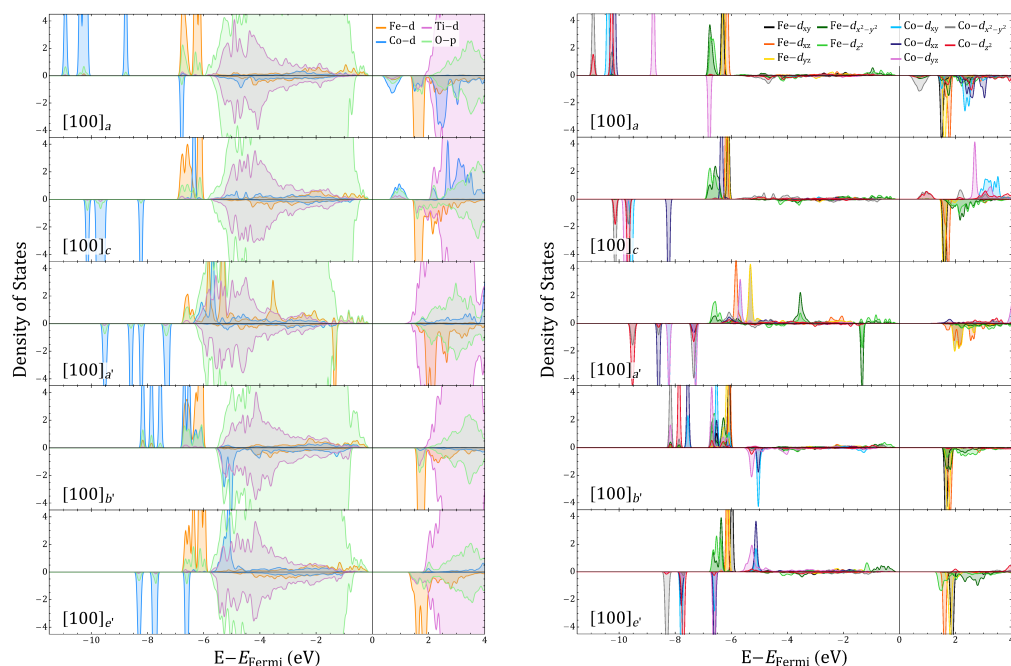


Figure A12. Fe, Co, Ti *d*-orbital and O *p*-orbital (left panel) and Fe, Co *d*-suborbital (right panel) projected density of states for $[100]_{a,c}$ and $[100]_{a',b',e'}$ vacancies corresponding to δ_{01} and δ_{02} , respectively.

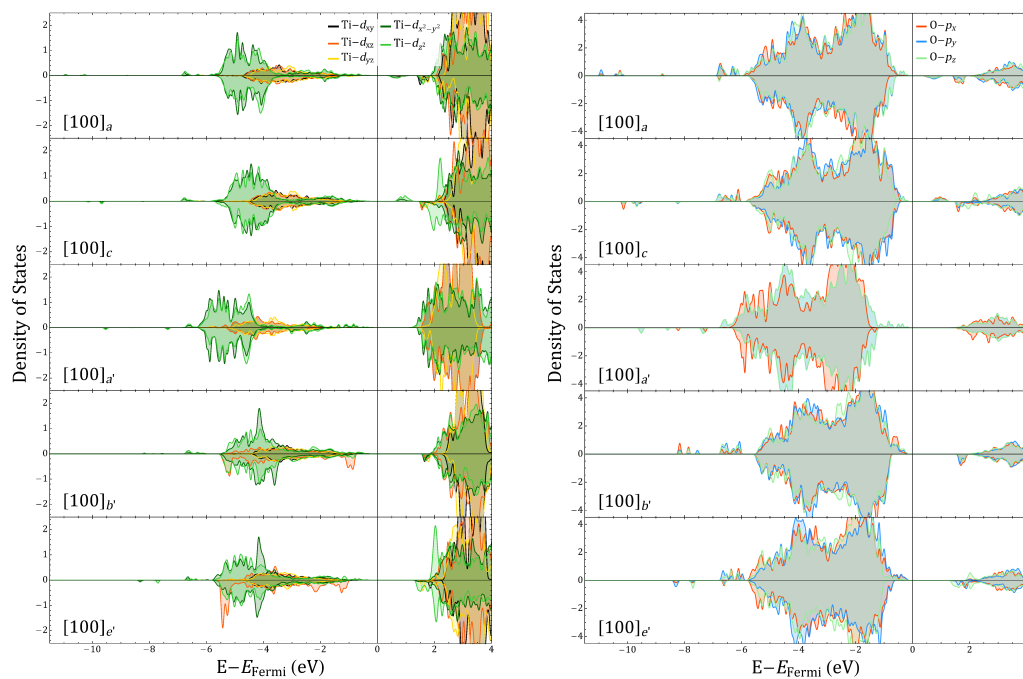


Figure A13. Ti *d*-suborbital (left panel) and O *p*-suborbital (right panel) projected density of states for $[100]_{a,c}$ and $[100]_{a',b',e'}$ vacancies corresponding to δ_{01} and δ_{02} , respectively.

Appendix E. Robustness against Different Functionals

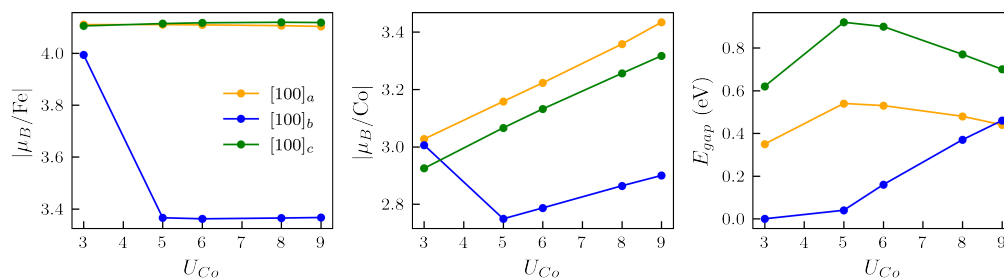


Figure A14. Fe/Co magnetic moments magnitude and band gap of δ_{01} configurations for different $+U$ parameters. U_{Co} was tuned down to 3 eV while keeping $(U_{Fe}, U_{Ti}) = (3, 8)$.

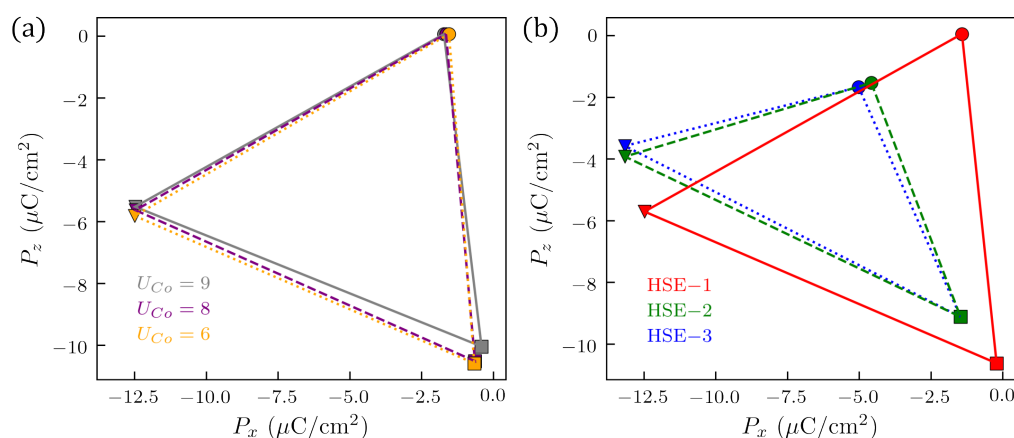


Figure A15. Polarization of δ_{01} configurations tested against (a) different $+U$ parameters and (b) the HSE06 hybrid functional. $[100]_a$ is represented by circles, $[100]_b$ by squares, and $[100]_c$ by triangles, following the same scheme as in Figure 2a,b. For a clear comparison, we show a region corresponding to only one of the “polarization triangles” of Figure 2a. U_{Co} was decreased from 9 to 3 eV while keeping $(U_{Fe}, U_{Ti}) = (3, 8)$. Hybrid calculations were carried starting from the GGA+U structures; HSE-1 maintains the structure rigid while constraining magnetization to the values presented in Table 1; in HSE-2, the structure is allowed to relax, followed by a constrained magnetization calculation. For HSE-3, both structure and magnetization are relaxed.

References

- Spaldin, N.A.; Ramesh, R. Advances in magnetoelectric multiferroics. *Nat. Mater.* **2019**, *18*, 203. [[CrossRef](#)] [[PubMed](#)]
- Fiebig, M.; Lottermoser, T.; Meier, D.; Trassin, M. The evolution of multiferroics. *Nat. Rev. Mater.* **2016**, *1*, 16046. [[CrossRef](#)]
- Marthinsen, A.; Faber, C.; Aschauer, U.; Spaldin, N.A.; Selbach, S.M. Coupling and competition between ferroelectricity, magnetism, strain, and oxygen vacancies in AMnO₃ perovskites. *MRS Commun.* **2016**, *6*, 182. [[CrossRef](#)]
- Goto, T.; Kim, D.H.; Sun, X.; Onbasli, M.C.; Florez, J.M.; Ong, S.P.; Vargas, P.; Ackland, K.; Stamenov, P.; Aimon, N.M.; et al. Magnetism and Faraday Rotation in Oxygen-Deficient Polycrystalline and Single-Crystal Iron-Substituted Strontium Titanate. *Phys. Rev. Appl.* **2017**, *7*, 024006. [[CrossRef](#)]
- Florez, J.M.; Ong, S.P.; Onbasli, M.C.; Dionne, G.F.; Vargas, P.; Ceder, G.; Ross, C.A. First-principles insights on the magnetism of cubic SrTi_{1-x}Co_xO_{3-δ}. *Appl. Phys. Lett.* **2012**, *100*, 252904. [[CrossRef](#)]
- Tang, A.S.; Onbasli, M.C.; Sun, X.; Ross, C.A. Thickness-Dependent Double-Epitaxial Growth in Strained SrTi_{0.7}Co_{0.3}O_{3-δ} Films. *ACS Appl. Mater. Interfaces* **2018**, *10*, 7469. [[CrossRef](#)]
- Pai, Y.; Tylan-Tyler, A.; Irvin, P.; Levy, J. Physics of SrTiO₃-based heterostructures and nanostructures: A review. *Rep. Prog. Phys.* **2018**, *81*, 036503. [[CrossRef](#)]
- Aschauer, U.; Spaldin, N.A. Competition and cooperation between antiferrodistortive and ferroelectric instabilities in the model perovskite SrTiO₃. *J. Phys. Condens. Matter* **2014**, *26*, 122203. [[CrossRef](#)]
- Shin, D.; Latini, S.; Schäfer, C.; Sato, S.A.; Giovannini, U.D.; Hübener, H.; Rubio, A. Quantum Paraelectric Phase of SrTiO₃ from First Principles. *Phys. Rev. B* **2021**, *104*, L060103. [[CrossRef](#)]
- Latini, S.; Shin, D.; Sato, S.A.; Schäfer, C.; Giovannini, U.D.; Hübener, H.; Rubio, A. The Ferroelectric Photo Ground State of SrTiO₃: Cavity Materials Engineering. *Proc. Natl. Acad. Sci. USA* **2021**, *118*, e2105618118. [[CrossRef](#)]

11. Xu, T.; Shimada, T.; Mori, M.; Fujimoto, G.; Wang, J.; Kitamura, T. Defect Engineering for Nontrivial Multiferroic Orders in SrTiO₃. *Phys. Rev. Mater.* **2020**, *4*, 124405. [[CrossRef](#)]
12. Hemberger, J.; Lunkenheimer, P.; Viana, R.; Böhrer, R.; Loidl, A. Electric-field-dependent dielectric constant and nonlinear susceptibility in SrTiO₃. *Phys. Rev. B* **1995**, *52*, 13159. [[CrossRef](#)] [[PubMed](#)]
13. Haeni, J.H.; Irvin, P.; Chang, W.; Uecker, R.; Reiche, P.; Li, Y.L.; Choudhury, S.; Tian, W.; Hawley, M.E.; Craigo, B.; et al. Room-temperature ferroelectricity in strained SrTiO₃. *Nature* **2004**, *430*, 758. [[CrossRef](#)] [[PubMed](#)]
14. Kim, Y.S.; Kim, D.J.; Kim, T.H.; Noh, T.W.; Choi, J.S.; Park, B.H.; Yoon, J.-G. Observation of room-temperature ferroelectricity in tetragonal strontium titanate thin films on SrTiO₃ (001) substrates. *Appl. Phys. Lett.* **2007**, *91*, 042908. [[CrossRef](#)]
15. Jang, H.W.; Kumar, A.; Denev, S.; Biegalski, M.D.; Maksymovych, P.; Bark, C.W.; Nelson, C.T.; Folkman, C.M.; Baek, S.H.; Balke, N.; et al. Ferroelectricity in Strain-Free SrTiO₃ Thin Films. *Phys. Rev. Lett.* **2010**, *104*, 197601. [[CrossRef](#)]
16. Choi, M.; Oba, F.; Tanaka, I. Role of Ti Antisitelike Defects in SrTiO₃. *Phys. Rev. Lett.* **2009**, *103*, 185502. [[CrossRef](#)]
17. Kim, Y.S.; Kim, J.; Moon, S.J.; Choi, W.S.; Chang, Y.J.; Yoon, J.-G.; Yu, J.; Chung, J.-S.; Noh, T.W. Localized electronic states induced by defects and possible origin of ferroelectricity in strontium titanate thin films. *Appl. Phys. Lett.* **2009**, *94*, 202906. [[CrossRef](#)]
18. Klyukin, K.; Alexandrov, V. Effect of intrinsic point defects on ferroelectric polarization behavior of SrTiO₃. *Phys. Rev. B* **2017**, *95*, 035301. [[CrossRef](#)]
19. Yang, F.; Zhang, Q.; Yang, Z.; Gu, J.; Liang, Y.; Li, W.; Wang, W.; Jin, K.; Gu, L.; Guo, J. Room-temperature ferroelectricity of SrTiO₃ films modulated by cation concentration. *Appl. Phys. Lett.* **2015**, *107*, 082904. [[CrossRef](#)]
20. Sokolovic, I.; Schmid, M.; Diebold, U.; Setvin, M. Incipient ferroelectricity: A route towards bulk-terminated. *Phys. Rev. Mater.* **2019**, *3*, 034407. [[CrossRef](#)]
21. Hallsteinsen, I.; Nord, M.; Bolstad, T.; Vullum, P.-E.; Boschker, J.E.; Longo, P.; Takahashi, R.; Holmestad, R.; Lippmaa, M.; Tybell, T. Effect of Polar (111)-Oriented SrTiO₃ on Initial Perovskite Growth. *Cryst. Growth Des.* **2016**, *16*, 2357. [[CrossRef](#)]
22. Xu, T.; Shimada, T.; Araki, Y.; Wang, J.; Kitamura, T. Multiferroic Domain Walls in Ferroelectric PbTiO₃ with Oxygen Deficiency. *Nano Lett.* **2015**, *16*, 454–458. [[CrossRef](#)] [[PubMed](#)]
23. Lee, K.; Park, K.; Lee, H.J.; Song, M.S.; Lee, K.C.; Namkung, J.; Lee, J.H.; Park, J.; Chae, S.C. Enhanced ferroelectric switching speed of Si-doped HfO₂ thin film tailored by oxygen deficiency. *Sci. Rep.* **2021**, *11*, 6290. [[CrossRef](#)] [[PubMed](#)]
24. Cheng, S.; Li, M.; Deng, S.; Bao, S.; Tang, P.; Duan, W.; Ma, J.; Nan, C.; Zhu, J. Manipulation of Magnetic Properties by Oxygen Vacancies in Multiferroic YMnO₃. *Adv. Funct. Mater.* **2016**, *26*, 3589–3598. [[CrossRef](#)]
25. Agrawal, P.; Guo, J.; Yu, P.; Hebert, C.; Passerone, D.; Erni, R.; Rossell, M.D. Strain-driven oxygen deficiency in multiferroic SrMnO₃ thin films. *Phys. Rev. B* **2016**, *94*, 104101. [[CrossRef](#)]
26. Glinchuk, M.D.; Eliseev, E.A.; Li, G.; Zeng, J.; Kalinin, S.V.; Morozovska, A.N. Ferroelectricity induced by oxygen vacancies in relaxors with perovskite structure. *Phys. Rev. B* **2018**, *98*, 094102. [[CrossRef](#)]
27. Abd El-Naser, A.; Abdel-Khalek, E.K.; Nabhan, E.; Rayan, D.A.; Gaafar, M.S.; Abd El-Aal, N.S. Study the influence of oxygen-deficient ($\delta = 0.135$) in SrFeO_{3- δ} nanoparticles perovskite on structural, electrical and magnetic properties. *Philos. Mag.* **2020**, *101*, 710–728. [[CrossRef](#)]
28. Wang, Y.-G.; Tang, X.-G.; Liu, Q.-X.; Jiang, Y.-P.; Jiang, L.-L. Room Temperature Tunable Multiferroic Properties in Sol-Gel-Derived Nanocrystalline Sr(Ti_{1-x}Fe_x)O_{3- δ} Thin Films. *Nanomaterials* **2017**, *7*, 264. [[CrossRef](#)]
29. Wang, X.; Wang, Z.; Hu, Q.; Zhang, C.; Wang, D.; Li, L. Room temperature multiferroic properties of Fe-doped nonstoichiometric SrTiO₃ ceramics at both A and B sites. *Solid State Commun.* **2019**, *289*, 22. [[CrossRef](#)]
30. Florez, J.M.; Onbasli, M.C.; Kim, D.H.; Ong, S.P.; Ceder, G.; Vargas, P.; Ross, C.A. Abstract: M32.00014, APS March Meeting 2015, 2015; Volume 60, Number 1. Available online: <http://meetings.aps.org/link/BAPS.2015.MAR.M32.14> (accessed on 31 December 2021).
31. Mitra, C.; Lin, C.; Posadas, A.B.; Demkov, A.A. Role of Oxygen Vacancies in Room-Temperature Ferromagnetism in Cobalt-Substituted SrTiO₃. *Phys. Rev. B* **2014**, *90*, 125130. [[CrossRef](#)]
32. Posadas, A.B.; Mitra, C.; Lin, C.; Dhamdhere, A.; Smith, D.J.; Tsoi, M.; Demkov, A.A. Oxygen Vacancy-Mediated Room-Temperature Ferromagnetism in Insulating Cobalt-Substituted SrTiO₃ Epitaxially Integrated with Silicon. *Phys. Rev. B* **2013**, *87*, 144422. [[CrossRef](#)]
33. Sluchinskaya, I.A.; Lebedev, A.I. Cobalt in Strontium Titanate as a New Off-Center Magnetic Impurity. *Phys. Solid State* **2019**, *61*, 390. [[CrossRef](#)]
34. Opazo, M.A.; Ong, S.P.; Vargas, P.; Ross, C.A.; Florez, J.M. Oxygen-vacancy tuning of magnetism in SrTi_{0.75}Fe_{0.125}Co_{0.125}O_{3- δ} perovskite. *Phys. Rev. Mater.* **2019**, *3*, 014404. [[CrossRef](#)]
35. Liu, Y.; Baumann, S.; Schulze-Küppers, F.; Mueller, D.N.; Guillon, O. Co and Fe co-doping influence on functional properties of SrTiO₃ for use as oxygen transport membranes. *J. Eur. Ceram. Soc.* **2018**, *38*, 5058. [[CrossRef](#)]
36. Phoon, B.L.; Lai, C.W.; Juan, J.C.; Show, P.L.; Chen, W.H. A review of synthesis and morphology of SrTiO₃ for energy and other applications. *Int. J. Energy Res.* **2019**, *43*, 5151. [[CrossRef](#)]
37. Mroziński, A.; Molin, S.; Karczewski, J.; Miruszewski, T.; Jasiński, P. Electrochemical properties of porous Sr_{0.86}Ti_{0.65}Fe_{0.35}O₃ oxygen electrodes in solid oxide cells: Impedance study of symmetrical electrodes. *Int. J. Hydrogen Energy* **2019**, *44*, 1827. [[CrossRef](#)]
38. Kim, D.H.; Aimon, N.M.; Bi, L.; Florez, J.M.; Dionne, G.F.; Ross, C.A. Magnetostriction in epitaxial SrTi_{1-x}Fe_xO_{3- δ} perovskite films with x = 0.13 and 0.35. *J. Phys. Condens. Matter* **2013**, *25*, 026002. [[CrossRef](#)]

39. Ning, S.; Zhang, Q.; Occhialini, C.; Comin, R.; Zhong, X.; Ross, C.A. Voltage Control of Magnetism above Room Temperature in Epitaxial $\text{SrCo}_{1-x}\text{Fe}_x\text{O}_{3-\delta}$. *ACS Nano* **2020**, *14*, 8949. [CrossRef]
40. Inkinen, S.; Yao, L.; van Dijken, S. Reversible Thermal Strain Control of Oxygen Vacancy Ordering in an Epitaxial $\text{La}_{0.5}\text{Sr}_{0.5}\text{CoO}_{3-\delta}$ Film. *Phys. Rev. Mater.* **2020**, *4*, 046002. [CrossRef]
41. Assat, G.; Tarascon, J.-M. Fundamental understanding and practical challenges of anionic redox activity in Li-ion batteries. *Nat. Energy* **2018**, *3*, 373. [CrossRef]
42. Myeong, S.; Cho, W.; Jin, W.; Hwang, J.; Yoon, M.; Yoo, Y.; Nam, G.; Jang, H.; Han, J.-G.; Choi, N.-S.; et al. Understanding voltage decay in lithium-excess layered cathode materials through oxygen-centred structural arrangement. *Nat. Commun.* **2018**, *9*, 3285. [CrossRef] [PubMed]
43. Rawat, K.; Fong, D.D.; Aidhy, D.S. Breaking Atomic-Level Ordering via Biaxial Strain in Functional Oxides: A DFT Study. *J. Appl. Phys.* **2021**, *129*, 095301. [CrossRef]
44. Iijima, S.; Yang, W.; Matsumura, S.; Ohnishi, I. Atomic Resolution Imaging of Cation Ordering in Niobium–Tungsten Complex Oxides. *Commun Mater* **2021**, *2*, 1. [CrossRef]
45. Kresse, G.; Furthmüller, J. Efficient iterative schemes for ab initio total-energy calculations using a plane-wave basis set. *Phys. Rev. B* **1996**, *54*, 11169. [CrossRef]
46. Kresse, G.; Joubert, D. From ultrasoft pseudopotentials to the projector augmented-wave method. *Phys. Rev. B* **1999**, *59*, 1758. [CrossRef]
47. Jonsson, H.; Mills, G.; Jacobsen, K.W. Nudged elastic band method for finding minimum energy paths of transitions. In *Classical and Quantum Dynamics in Condensed Phase Simulations*; Berne, B.J., Ciccotti, G., Coker, D.F., Eds.; World Scientific: Singapore, 1998.
48. Rohrbach, A.; Hafner, J.; Kresse, G. Electronic correlation effects in transition-metal sulfides. *J. Phys. Condens. Matter* **2003**, *15*, 979. [CrossRef]
49. Heyd, J.; Scuseria, G.E.; Ernzerhof, M. Hybrid functionals based on a screened Coulomb potential. *J. Chem. Phys.* **2003**, *118*, 8207. [CrossRef]
50. Resta, R. Macroscopic polarization in crystalline dielectrics: The geometric phase approach. *Rev. Mod. Phys.* **1994**, *66*, 899. [CrossRef]
51. Zhou, W.X.; Ariando, A. Review on Ferroelectric/Polar Metals. *Jpn. J. Appl. Phys.* **2020**, *59*, S10802. [CrossRef]
52. Hadjimichael, M.; Li, Y.; Zatterin, E.; Chahine, G.A.; Conroy, M.; Moore, K.; Connell, E.N.O.; Ondrejko, P.; Marton, P.; Hlinka, J.; et al. Metal–Ferroelectric Supercrystals with Periodically Curved Metallic Layers. *Nat. Mater.* **2021**, *20*, 4. [CrossRef] [PubMed]
53. Momma, K.; Izumi, F. VESTA 3 for Three-Dimensional Visualization of Crystal, Volumetric and Morphology Data. *J. Appl. Cryst.* **2011**, *44*, 1272. [CrossRef]
54. Palmer, D.C. *CrystalMaker*; CrystalMaker Software Ltd.: Oxfordshire, UK, 2014. Available online: www.crystallmaker.com (accessed on 31 December 2021).
55. Ong, S.P.; Richards, W.D.; Jain, A.; Hautier, G.; Kocher, M.; Cholia, S.; Gunter, D.; Chevrier, V.L.; Persson, K.A.; Ceder, G. Python Materials Genomics (pymatgen): A robust, open-source python library for materials analysis. *Comput. Mater. Sci.* **2013**, *68*, 314. [CrossRef]
56. Makov, G.; Payne, M.C. Periodic boundary conditions in ab initio calculations. *Phys. Rev. B* **1995**, *51*, 4014. [CrossRef] [PubMed]
57. Emery, A.A.; Wolverton, C. High-Throughput DFT Calculations of Formation Energy, Stability and Oxygen Vacancy Formation Energy of ABO₃ Perovskites. *Sci. Data* **2017**, *4*, 1. [CrossRef] [PubMed]
58. Tahini, H.A.; Tan, X.; Schwingschlögl, U.; Smith, S.C. Formation and Migration of Oxygen Vacancies in SrCoO₃ and Their Effect on Oxygen Evolution Reactions. *ACS Catal.* **2016**, *6*, 5565. [CrossRef]
59. Wang, L.; Maxisch, T.; Ceder, G. Oxidation energies of transition metal oxides within the GGA+U framework. *Phys. Rev. B* **2006**, *73*, 195107. [CrossRef]
60. Lee, Y.-L.; Kleis, J.; Rossmeis, J.; Morgan, D. Ab initio energetics of LaBO₃ (001) (B = Mn, Fe, Co, and Ni) for solid oxide fuel cell cathodes. *Phys. Rev. B* **2009**, *80*, 224101. [CrossRef]
61. Hombo, J.; Matsumoto, Y.; Kawano, T. Electrical conductivities of SrFeO_{3-δ} and BaFeO_{3-δ} perovskites. *J. Solid State Chem.* **1990**, *84*, 138. [CrossRef]
62. Jahn, H.A.; Teller, E. Stability of Polyatomic Molecules in Degenerate Electronic States—I—Orbital Degeneracy, Proceedings of the Royal Society of London. *Ser.-Math. Phys. Sci.* **1937**, *161*, 220.
63. Tkacz-Śmiech, K.; Koleżyński, A.; Ptak, W.S. Chemical Bond in Ferroelectric Perovskites. *Ferroelectrics* **2000**, *237*, 57. [CrossRef]
64. Xu, S.; Jacobs, R.; Morgan, D. Factors Controlling Oxygen Interstitial Diffusion in the Ruddlesden-Popper Oxide La_{2-x}Sr_xNiO_{4+δ}. *Chem. Mater.* **2018**, *30*, 7166. [CrossRef]
65. Resta, R.; Vanderbilt, D. Theory of Polarization: A Modern Approach. *Top. Appl. Phys.* **2007**, *105*, 31–61.
66. Vanderbilt, D. *Berry Phases in Electronic Structure Theory: Electric Polarization, Orbital Magnetization and Topological Insulators*; Cambridge University Press: Cambridge, UK, 2018.
67. Jadaun, P.; Xiao, D.; Niu, Q.; Banerjee, S.K. Topological classification of crystalline insulators with space group symmetry. *Phys. Rev. B* **2013**, *88*, 085110. [CrossRef]
68. Raeliarijaona, A.; Fu, H. Persistence of strong and switchable ferroelectricity despite vacancies. *Sci. Rep.* **2017**, *7*, 41301. [CrossRef] [PubMed]

69. Zhang, B.H.; Liu, X.Q.; Chen, X.M. Review of experimental progress of hybrid improper ferroelectricity in layered perovskite oxides. *J. Phys. D Appl. Phys.* **2022**, *55*, 113001. [[CrossRef](#)]
70. Reyes-Lillo, S.E.; Rabe, K.M.; Neaton, J.B. Ferroelectricity in [111]-oriented epitaxially strained SrTiO₃ from first principles. *Phys. Rev. Mater.* **2019**, *3*, 030601. [[CrossRef](#)]
71. Ritzmann, A.M.; noz-García, A.B.M.; Pavone, M.; Keith, J.A.; Carter, E.A. Ab Initio DFT+U Analysis of Oxygen Vacancy Formation and Migration in La_{1-x}Sr_xFeO_{3-δ} ($x = 0, 0.25, 0.50$). *Chem. Mater.* **2013**, *25*, 3011. [[CrossRef](#)]
72. Tahini, H.A.; Tan, X.; Lou, S.N.; Scott, J.; Amal, R.; Ng, Y.H.; Smith, S.C. Mobile Polaronic States in α -MoO₃: An ab Initio Investigation of the Role of Oxygen Vacancies and Alkali Ions. *ACS Appl. Mater. Interfaces* **2016**, *8*, 10911. [[CrossRef](#)]
73. He, X.; Mo, Y. Accelerated materials design of Na_{0.5}Bi_{0.5}TiO₃ oxygen ionic conductors based on first principles calculations. *Phys. Chem. Chem. Phys.* **2015**, *17*, 18035. [[CrossRef](#)]
74. Chroneos, A.; Vovk, R.V.; Goulatis, I.L.; Goulatis, L.I. Oxygen transport in perovskite and related oxides: A brief review. *J. Alloys Compd.* **2010**, *494*, 190. [[CrossRef](#)]
75. Souza, R.A.D. Oxygen Diffusion in SrTiO₃ and Related Perovskite Oxides. *Adv. Funct. Mater.* **2015**, *25*, 6326. [[CrossRef](#)]
76. Mayeshiba, T.T.; Morgan, D.D. Factors controlling oxygen migration barriers in perovskites. *Solid State Ion.* **2016**, *296*, 71. [[CrossRef](#)]
77. Vives, S.; Meunier, C. Defect cluster arrangements and oxygen vacancy migration in Gd doped ceria for different interatomic potentials. *Solid State Ion.* **2015**, *283*, 137. [[CrossRef](#)]
78. Souza, R.A.D.; Ramadan, A.; Hörner, S. Modifying the barriers for oxygen-vacancy migration in fluorite-structured CeO₂ electrolytes through strain: A computer simulation study. *Energy Environ. Sci.* **2012**, *5*, 5445. [[CrossRef](#)]
79. Kong, F.; Liang, C.; Wang, L.; Zheng, Y.; Perananthan, S.; Longo, R.C.; Ferraris, J.P.; Kim, M.; Cho, K. Kinetic Stability of Bulk LiNiO₂ and Surface Degradation by Oxygen Evolution in LiNiO₂-Based Cathode Materials. *Adv. Energy Mater.* **2019**, *9*, 1802586. [[CrossRef](#)]
80. Goikoetxea, J.; Friedrich, C.; Bihlmayer, G.; Blügel, S.; Arnau, A.; Blanco-Rey, M. Multiplet effects in the electronic correlation of one-dimensional magnetic transition metal oxides on metals. *Phys. Rev. B* **2022**, *106*, 035130. [[CrossRef](#)]
81. Allen, J.P.; Watson, G.W. Occupation matrix control of d- and f-electron localisations using DFT + U. *Phys. Chem. Chem. Phys.* **2014**, *16*, 21016. [[CrossRef](#)]
82. Lü, W.; Li, C.; Zheng, L.; Xiao, J.; Lin, W.; Li, Q.; Wang, X.R.; Huang, Z.; Zeng, S.; Han, K.; et al. Multi-Nonvolatile State Resistive Switching Arising from Ferroelectricity and Oxygen Vacancy Migration. *Adv. Mater.* **2017**, *29*, 1606165. [[CrossRef](#)]
83. Liao, Z.; Gao, P.; Bai, X.; Chen, D.; Zhang, J. Evidence for electric-field-driven migration and diffusion of oxygen vacancies in Pr_{0.7}Ca_{0.3}MnO₃. *J. Appl. Phys.* **2012**, *111*, 114506. [[CrossRef](#)]
84. Hanzig, J.; Mehner, E.; Jachalke, S.; Hanzig, F.; Zschornak, M.; Richter, C.; Leisegang, T.; Stöcker, H.; Meyer, D.C. Dielectric to pyroelectric phase transition induced by defect migration. *New J. Phys.* **2015**, *17*, 023036. [[CrossRef](#)]
85. Leighton, C. Electrolyte-based ionic control of functional oxides. *Nat. Mater.* **2019**, *18*, 13. [[CrossRef](#)] [[PubMed](#)]
86. Lee, J.; Ahn, E.; Seo, Y.-S.; Kim, Y.; Jeon, T.-Y.; Cho, J.; Lee, I.; Jeon, H. Redox-Driven Nanoscale Topotactic Transformations in Epitaxial SrFe_{0.8}Co_{0.2}O_{3-x} under Atmospheric Pressure. *Phys. Rev. Appl.* **2018**, *10*, 054035. [[CrossRef](#)]
87. Ishiwata, S.; Tokunaga, M.; Kaneko, Y.; Okuyama, D.; Tokunaga, Y.; Wakimoto, S.; Kakurai, K.; Arima, T.; Taguchi, Y.; Tokura, Y. Versatile helimagnetic phases under magnetic fields in cubic perovskite SrFeO₃. *Phys. Rev. B* **2011**, *84*, 5. [[CrossRef](#)]
88. Kinoshita, M.; Sakai, H.; Hayashi, N.; Tokura, Y.; Takano, M.; Ishiwata, S. Contrasting Magnetic Behaviors in Rhodium- and Ruthenium-Doped Cubic Perovskite SrFeO₃: Nearly Ferromagnetic Metal versus Spin-Glass Insulator. *Angew. Chem. Int. Ed.* **2016**, *55*, 49. [[CrossRef](#)] [[PubMed](#)]
89. Long, Y.; Kaneko, Y.; Ishiwata, S.; Taguchi, Y.; Tokura, Y. Synthesis of cubic SrCoO₃ single crystal and its anisotropic magnetic and transport properties. *J. Phys. Condens. Matter* **2011**, *23*, 24. [[CrossRef](#)]
90. Kim, D.H.; Bi, L.; Jiang, P.; Dionne, G.F.; Ross, C.A. Magnetoelastic effects in SrTi_{1-x}M_xO₃ (M = Fe, Co, or Cr) epitaxial thin films. *Phys. Rev. B* **2011**, *84*, 014416. [[CrossRef](#)]
91. Bi, L.; Kim, H.-S.; Dionne, G.; Gerald, F.; Ross, C.A. Structure, magnetic properties and magnetoelastic anisotropy in epitaxial Sr(Ti_{1-x}Co_x)O₃ films. *New J. Phys.* **2010**, *12*, 4. [[CrossRef](#)]
92. Pascanut, C.; Dragoie, N.; Berthet, P. Magnetic and transport properties of cobalt-doped perovskites SrTi_{1-x}Co_xO₃ ($x \leq 0.5$). *J. Magn. Magn. Mater.* **2006**, *305*, 1. [[CrossRef](#)]